Environmental Research Letters

CrossMark

LETTER

Sunlight mediated seasonality in canopy structure and photosynthetic activity of Amazonian rainforests

Jian Bi[1,20], Yuri Knyazikhin[1,20], Sungho Choi[1], Taejin Park[1], Jonathan Barichivich[2], Philippe Ciais[3], Rong Fu[4], Sangram Ganguly[5], Forrest Hall[6], Thomas Hilker[7], Alfredo Huete[8], Matthew Jones[9], John Kimball[9], Alexei I Lyapustin[10], Matti Mõttus[11], Ramakrishna R Nemani[12], Shilong Piao[13,14], Benjamin Poulter[15], Scott R Saleska[16], Sassan S Saatchi[17,18], Liang Xu[17], Liming Zhou[19] and Ranga B Myneni[1]

1 Department of Earth and Environment, Boston University, Boston, MA 02215, USA
2 Climatic Research Unit, School of Environmental Sciences, University of East Anglia, Norwich NR4 7TJ, UK
3 Laboratoire des Sciences du Climat et de l'Environnement, IPSL-LSCE, CEA-CNRS-UVSQ, 91191 Gif sur Yvette Cedex, France
4 Department of Geological Sciences, The University of Texas at Austin, Austin, TX 78712, USA
5 Bay Area Environmental Research Institute, NASA Ames Research Center, Moffett Field, CA 94035, USA
6 Biospheric Sciences Laboratory, NASA Goddard Space Flight Center, Greenbelt, MD 20771, USA
7 College of Forestry, Oregon State University, Corvallis, OR 97331, USA
8 Plant Functional Biology and Climate Change Cluster, University of Technology Sydney, New South Wales 2007, Australia
9 Numerical Terradynamic Simulation Group, The University of Montana, Missoula, MT 59812, USA
10 Climate and Radiation Laboratory, NASA Goddard Space Flight Center, Greenbelt, MD 20771, USA
11 Department of Geosciences and Geography, University of Helsinki, FI-00014, Helsinki, Finland
12 NASA Advanced Supercomputing Division, Ames Research Center, Moffett Field, California 94035, USA
13 Department of Ecology, Peking University, Beijing 100871, People's Republic of China
14 Institute of Tibetan Plateau Research, Chinese Academy of Sciences, Beijing 100085, People's Republic of China
15 Department of Ecology, Montana State University, Bozeman, MT 59717, USA
16 Department of Ecology and Evolutionary Biology, University of Arizona, Tucson, AZ 85721, USA
17 Institute of the Environment and Sustainability, University of California, Los Angeles, CA 90095, USA
18 Radar Science and Engineering section, Jet Propulsion Laboratory, California Institute of Technology, Pasadena, CA 91109, USA
19 Department of Atmospheric and Environmental Sciences, University at Albany, State University of New York, Albany, New York 12222, USA
20 These authors contributed equally to this work.

E-mail: jknjazi@bu.edu

Abstract

Resolving the debate surrounding the nature and controls of seasonal variation in the structure and metabolism of Amazonian rainforests is critical to understanding their response to climate change. *In situ* studies have observed higher photosynthetic and evapotranspiration rates, increased litterfall and leaf flushing during the Sunlight-rich dry season. Satellite data also indicated higher greenness level, a proven surrogate of photosynthetic carbon fixation, and leaf area during the dry season relative to the wet season. Some recent reports suggest that rainforests display no seasonal variations and the previous results were satellite measurement artefacts. Therefore, here we re-examine several years of data from three sensors on two satellites under a range of sun positions and satellite measurement geometries and document robust evidence for a seasonal cycle in structure and greenness of wet equatorial Amazonian rainforests. This seasonal cycle is concordant with independent observations of solar radiation. We attribute alternative conclusions to an incomplete study of the seasonal cycle, i.e. the dry season only, and to prognostications based on a biased radiative transfer model. Consequently, evidence of dry season greening in geometry corrected satellite data was ignored and the absence of evidence for seasonal variation in lidar data due to noisy and saturated signals was misinterpreted as evidence of the absence of changes during the dry season. Our results, grounded in the physics of radiative transfer, buttress previous reports of dry season increases in leaf flushing, litterfall, photosynthesis and evapotranspiration in well-hydrated Amazonian rainforests.

1. Introduction

Understanding the seasonal variation in functioning of rainforests and its controls are requisite for understanding how rainforests will respond to climate change. *In situ* studies report counter-intuitive seasonal variation in wet equatorial Amazonian rainforests —higher photosynthetic and evapotranspiration rates and increased litterfall and leaf flushing during the Sunlight-rich dry season (Saleska *et al* 2003, da Rocha *et al* 2004, Goulden *et al* 2004, Rice *et al* 2004, Hasler and Avissar 2007, Hutyra *et al* 2007, Negrón Juárez *et al* 2009, Costa *et al* 2010, Jones *et al* 2014). Water limitation during the dry season is alleviated in these forests through deep roots and hydraulic redistribution (Nepstad *et al* 1994, Oliveira *et al* 2005). Satellite data, which cover a large area and span a long time period, support findings of *in situ* studies—higher radiometric greenness level and green leaf area during the dry season compared to the wet season (Xiao *et al* 2005, Huete *et al* 2006, Myneni *et al* 2007, Samanta *et al* 2012, Hilker *et al* 2014, Jones *et al* 2014, Maeda *et al* 2014). This convergent view of seasonality, parsed from several studies, shows how sunlight interacts with adaptive mechanisms to result in higher rates of leaf flushing, litterfall, photosynthesis and evapotranspiration in tropical forests if water limitation is absent (Wright and Van Schaik 1994, Restrepo-Coupe *et al* 2013, Borchert *et al* 2015, Guan *et al* 2015).

This community-consensual view was questioned in recent studies (Galvão *et al* 2011, Morton *et al* 2014). The studies claim that the dry season greening inferred from passive remote sensing data resulted from an artificial increase in forest canopy reflectance at near-infrared (NIR) wavelengths caused by variations in sun-satellite sensor geometry. Their analyses of satellite-borne lidar data suggested that these forests exhibited no seasonal variations in canopy structure or leaf area. Relying on model simulations to guide and imbue a physical meaning to the satellite data analysis, the studies conclude that Amazon rainforests maintain consistent structure and greenness during the dry season.

These contradictory results justify a re-examination of the same satellite data with the goal of assessing seasonality in wet equatorial Amazonian rainforests. In addition to data from NASA's Moderate Resolution Imaging Spectroradiometer (MODIS) on the Terra platform and the Geoscience Laser Altimeter System (GLAS) instrument onboard the Ice, Cloud and land Elevation Satellite (ICESat) used in (Morton *et al* 2014), we also include data from the MODIS instrument on Aqua and Multiangle Imaging Spectroradiometer (MISR) on the Terra satellite. The MISR sensor views the Earth's surface with nine cameras simultaneously, as opposed to the two MODIS sensors, which are capable of only one view each. This feature enables the rigorous use of the theory of radiative transfer in vegetation canopies—the fundamental

theory that explains from first principles the mechanisms underlying the signals generated by the canopy and measured by a remote sensor (Knyazikhin *et al* 2005).

This study is focused on terra firme rainforests in central Amazonia that are relatively undisturbed by human activities (supplementary data and methods section 1, figure S1). The period June to May is treated as one seasonal cycle as per convention (Huete *et al* 2006, Morton *et al* 2014). It consists of a short dry season, June to October, and a long wet season thereafter (supplementary data and methods section 1). The following analysis of satellite borne sensor data addresses the question at the center of current debate —did previous studies (Xiao *et al* 2005, Huete *et al* 2006, Myneni *et al* 2007, Brando *et al* 2010, Samanta *et al* 2012) misinterpret changes in near-infrared (NIR) reflectance caused by seasonal changes in sun-satellite sensor geometry (figures S2 and S3) as seasonal variations in rainforest canopy structure and greenness (Galvão *et al* 2011, Morton *et al* 2014)?

2. Data and methods

A detailed description of methods and data used is given in the supplementary information available at stacks.iop.org/ERL/10/064014/mmedia. A brief summary is provided here. The study region and the various data analysed in this study are detailed in the supplementary data and methods section 1–2. The sun-sensor geometry relevant to the discussion in this article is presented in the supplementary data and methods section 3. The theory of remote measurements and evaluation of NIR reflectance angular signatures (figure 3) and their interpretation is described in the supplementary data and methods section 4. A critical look at Morton *et al* 2014 analyses of MODIS and GLAS data is presented in the supplementary discussion. Abbreviations and symbols are listed in supplementary table S5.

3. Results and discussioin

3.1. Leaf area index seasonality

The seasonal cycle of green leaf area inferred from satellite data (figure 1(a)) exhibits rising values during the dry season (June to October), high values during the early part of the wet season (November to February) and decreasing values thereafter (March to May). This seasonal variation of about 20% is imposed on a base value of Leaf Area Index (LAI, one-sided green leaf area per unit ground area) of about 5.75, is greater than the uncertainty of the LAI product (0.66 LAI, Yang *et al* 2006) and is observed in nearly 70% of the rainforests in the study domain (figure S4(a)); the rest lacked valid data. Is this seasonal variation real or a misinterpretation of changes in satellite-sensor measurements caused by seasonal changes in sun position
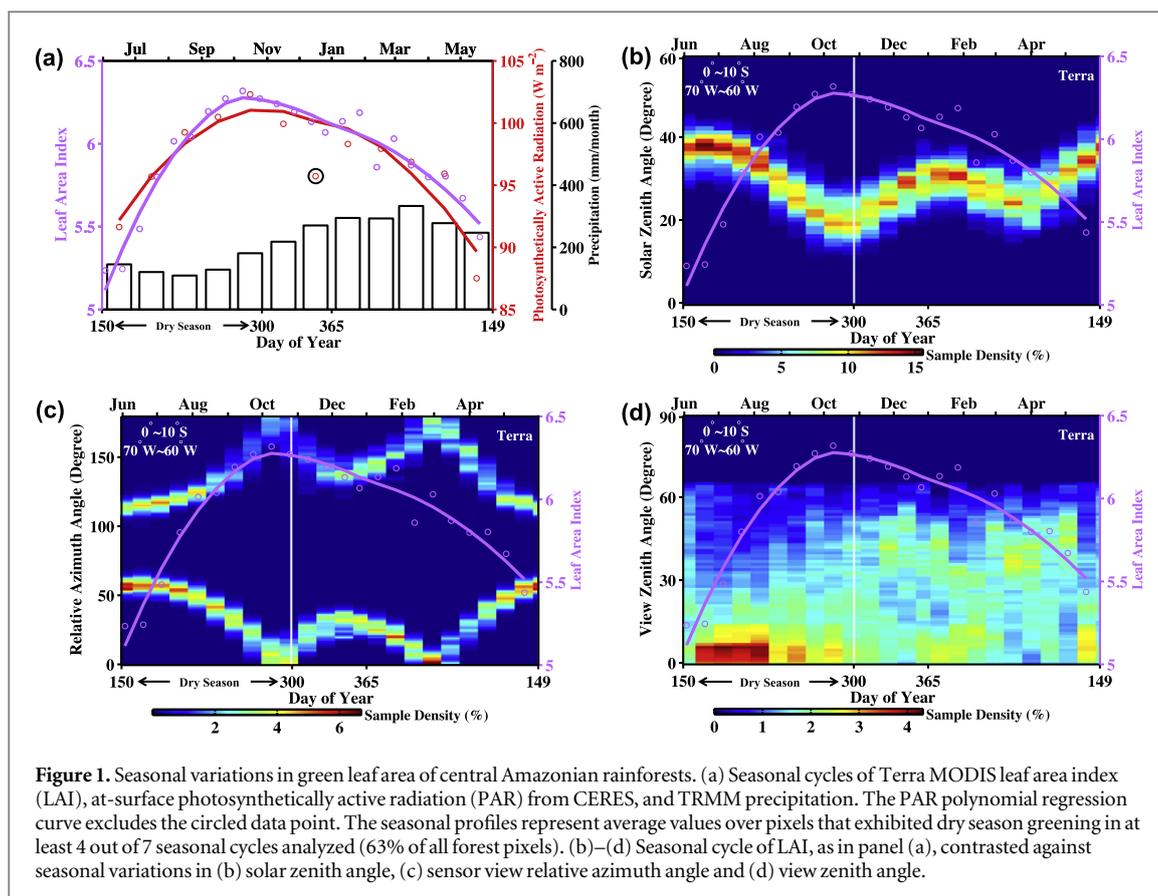
Figure 1. Seasonal variations in green leaf area of central Amazonian rainforests. (a) Seasonal cycles of Terra MODIS leaf area index (LAI), at-surface photosynthetically active radiation (PAR) from CERES, and TRMM precipitation. The PAR polynomial regression curve excludes the circled data point. The seasonal profiles represent average values over pixels that exhibited dry season greening in at least 4 out of 7 seasonal cycles analyzed (63% of all forest pixels). (b)–(d) Seasonal cycle of LAI, as in panel (a), contrasted against seasonal variations in (b) solar zenith angle, (c) sensor view relative azimuth angle and (d) view zenith angle.
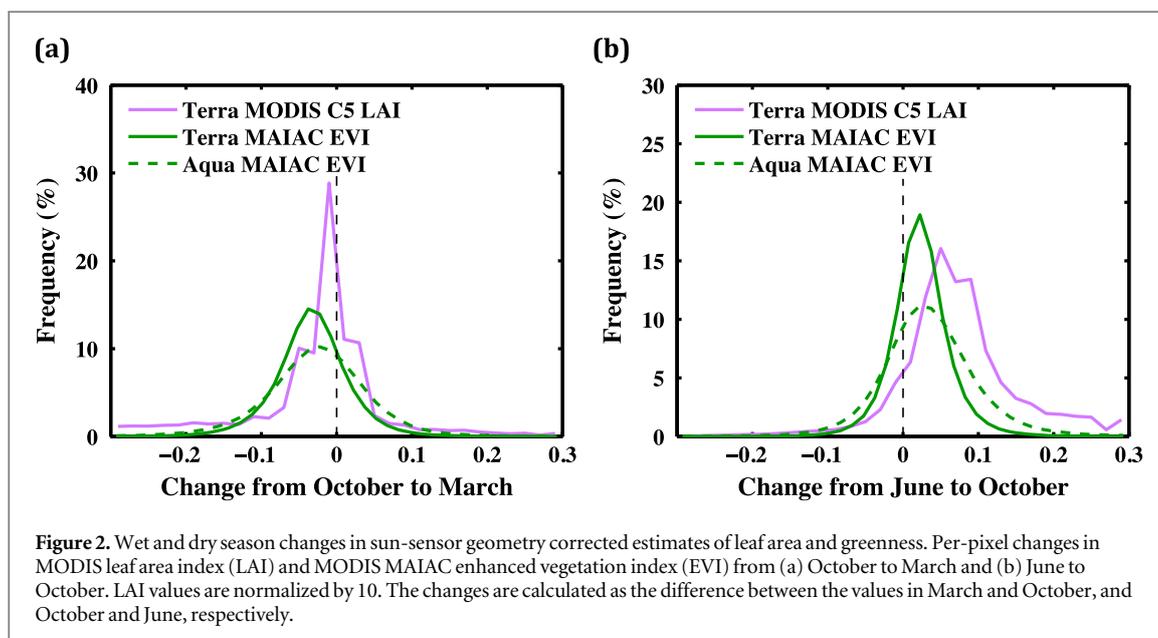
in the sky and the manner in which the sensor measures reflected radiation ('sun-sensor geometry')? The answer requires an understanding of how this geometry changes during the seasonal cycle, which is described in the supplementary data and methods section 3.

The seasonal cycle of leaf area in figure 1(a) cannot be an artefact of seasonal changes in sun-sensor geometry because the algorithm with which leaf area is derived explicitly accounts for geometry changes, i.e. the algorithm is capable of differentiating between changes in measurements caused by leaf area changes and those caused by geometry changes (Knyazikhin *et al* 1999, Knyazikhin *et al* 1998). This is also evident from the fact that the seasonal cycle of leaf area does not track the seasonal course of either the Sun position in the sky (figure 1(b)) or the MODIS sensor sampling (figures 1(c) and (d)). Instead, it tracks independently obtained observations of seasonal variation in sunlight (figure 1(a)). This behavior is consistent with the idea that sunlight acts as a proximate cue for leaf production in moist tropical forests if water limitation is absent (Wright and Van Schaik 1994, Borchert *et al* 2015, Guan *et al* 2015). Thus, relatively high sunlight levels from absence of clouds during the dry season cause leaf area to increase, which in turn generates higher rates of photosynthesis (Saleska *et al* 2003, Da Rocha *et al* 2004, Restrepo-Coupe *et al* 2013, Gatti *et al* 2014). But, photosynthesis becomes decoupled from sunlight during the early to middle part of the

wet season. This results in increasing rates of photosynthesis, which are possibly sustained by still sufficiently high levels of light and increasing leaf production (Restrepo-Coupe *et al* 2013). All three decrease rapidly thereafter. A bimodal seasonal cycle of LAI reported in one instance could be site-specific (figure 2 in Doughty and Goulden (2008)) as alternate *in situ* evidence does not exist (Restrepo-Coupe *et al* 2013, Xiao *et al* 2005, Asner *et al* 2000, Carswell *et al* 2002, Chave *et al* 2010, Malhado *et al* 2009, Negrón Juárez *et al* 2009).

3.2. Evidence for seasonality after sun-sensor geometry correction

The Enhanced Vegetation Index (EVI) is a proven proxy for the potential photosynthetic carbon fixation by vegetation (Xiao *et al* 2005, Huete *et al* 2006, Brando *et al* 2010). It is calculated from satellite-sensor measurements of reflected solar radiation at three different wavelength bands. These measurements depend on sun-sensor geometry, but this dependency can be eliminated by expressing the measurements in a fixed geometry (Morton *et al* 2014, Lyapustin *et al* 2012). The EVI calculated from MODIS sensor measurements in a fixed geometry, i.e. nadir viewing direction and 45° solar zenith angle, shows a distinct wet season decrease (figure 2(a)) and dry season increase (figure 2(b)). These changes are greater than a highly conservative estimate of the precision in 43% of the pixels during the wet season and 31% of the pixels

Figure 2. Wet and dry season changes in sun-sensor geometry corrected estimates of leaf area and greenness. Per-pixel changes in MODIS leaf area index (LAI) and MODIS MAIAC enhanced vegetation index (EVI) from (a) October to March and (b) June to October. LAI values are normalized by 10. The changes are calculated as the difference between the values in March and October, and October and June, respectively.

in the dry season. Here, the precision is estimated as the spatial standard deviation of the EVI data in the study domain. Analogous to EVI, pixel level estimates of green leaf area show a strong decrease in the wet season and increase during the dry season. The wet season decrease (figure 2(a)) suggests net leaf abscission, i.e. more older leaves dropped than those newly flushed, and the dry season increase indicates net leaf flushing (figure 2(b)), resulting in a sunlight mediated phenological behavior (Myneni *et al* 2007). The fact that both EVI and LAI show congruent changes during the seasonal cycle even though the Sun-sensor geometry effect is removed from measurements in different ways (Knyazikhin *et al* 1999, Knyazikhin *et al* 1998, Lyapustin *et al* 2012, Hilker *et al* 2014, Maeda *et al* 2014) is particularly noteworthy.
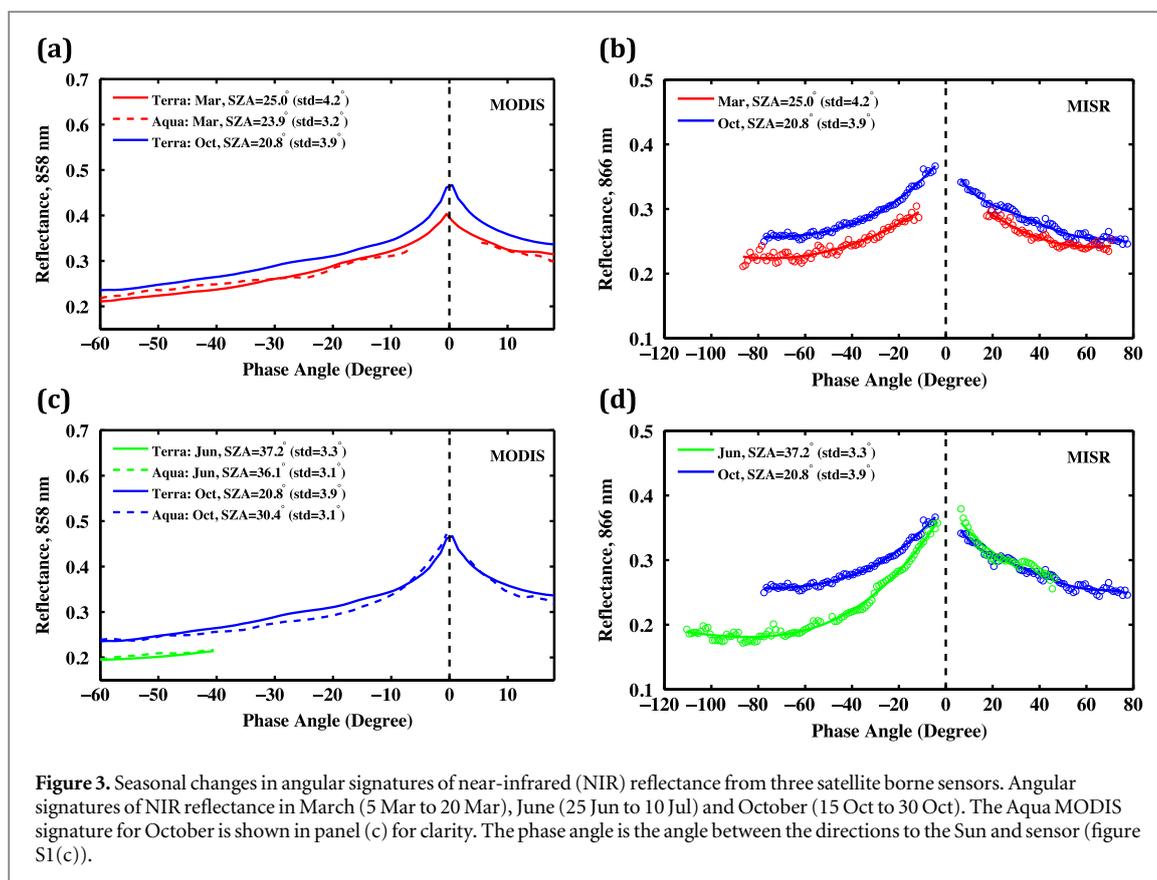
3.3. Evidence for seasonality from multiple sensors and geometries

Now we turn to satellite-sensor measurements of reflected solar radiation at the NIR wavelength band, which are at the heart of the controversy. These measurements are usually expressed as normalized quantities called reflectances (supplementary data and methods section 4.1–4.2). The geometric structure and radiation scattering properties of the rainforest canopy determine the magnitude and angular distribution of reflected radiation. The angular signatures of reflectance are therefore unique and rich sources of diagnostic information about rainforest canopies (Diner *et al* 1999). We first examine NIR angular signatures from the late dry season (October 15 to 30) and the middle part of the wet season (March 5 to 20). The Solar Zenith Angle (SZA) at the time when Terra (10:30 am) and Aqua (1:30 pm) satellites view the central Amazonian forests in March and October is between 20° and 30°. This variation minimally impacts the shape of angular signatures (supplementary data

and methods section 4.4). MODIS and MISR sensors sample the rainforests very differently (figures S2(c)–(f); also see figure S1(c)). However, all the sensors record a distinct decrease in reflected NIR radiation in all view directions between October and March with no change in the overall shape of the angular signatures (figures 3(a) and (b)). Such a simple change in magnitude can only result from a change in canopy properties—this conclusion is based on the physics of how solar radiation interacts with foliage in vegetation canopies (supplementary data and methods section 4.3, figures S5(a) and (b)). The EVI, although evaluated from reflectances at NIR, red and blue wavelength bands, is tightly linked to NIR reflectance (Samanta *et al* 2012). Thus, the decrease in sun-sensor geometry corrected EVI (figure 2(a)) is in agreement with directly observed decreases in NIR angular signatures from October to March (figures 3(a) and (b)).

The wet season reduction in greenness is inconsistent with the hypothesis of invariant dry season greenness. Indeed the net loss of leaf area, without a corresponding net gain elsewhere during the seasonal cycle, will result in rainforests without leaves in a few years. If wet Amazonian forests somehow maintain consistent canopy structure and greenness during the dry season, then they must be either aseasonal or the entire seasonal cycle must be confined to the wet season, but this argument lacks empirical support. The question then arises whether variations in angular signatures of forest reflectance during the dry season support this inference?

Therefore, let us now consider NIR reflectances from early (25 June to 10 July) and the late dry season (15 October to 30 October) when both sun position in the sky and sensor sampling vary significantly (figures S2(a)–(d); also see figure S1(c)). MODIS and MISR measurements are made at significantly higher SZA in June (~35°–40°) compared to October (~20°–30°).

Figure 3. Seasonal changes in angular signatures of near-infrared (NIR) reflectance from three satellite borne sensors. Angular signatures of NIR reflectance in March (5 Mar to 20 Mar), June (25 Jun to 10 Jul) and October (15 Oct to 30 Oct). The Aqua MODIS signature for October is shown in panel (c) for clarity. The phase angle is the angle between the directions to the Sun and sensor (figure S1(c)).

The magnitude and shape of angular signatures are impacted when both canopy properties and SZA vary. However, a higher or equal reflectance at lower SZA relative to reflectance at higher SZA always indicates an increase in leaf area and foliage scattering properties according to the physics of radiation interaction in vegetation (supplementary data and methods section 4.4–4.5, figures S5(c)−(f)). This is observed clearly in MISR data (figure 3(d)) because this sensor views the Earth's surface with nine cameras simultaneously, as opposed to the two MODIS sensors (figure 3(c)), which are capable of only one view each (figure S3). Further, the juxtaposition of the two angular signatures in figure 3(d) is significantly different than that predicted by theory for the case of identical canopies (supplementary data and methods section 4.6). Thus, the NIR angular signatures in figure 3(d) indicate a change in vegetation structure (LAI) and greenness (EVI) during the dry season.

4. Conclusions

Satellite data indicate a distinct sunlight-mediated seasonality in leaf area and photosynthetic carbon fixation over unstressed rainforests in central Amazonia. This seasonal cycle is not an artefact of seasonal changes in sun position in the sky or how the satellite-sensor measures the reflected radiation field. The spatially expansive remote sensing data agree with available *in situ* data. A better understanding of how

the rainforests will respond to climate change depends on future ground campaigns as satellite data can complement, but not substitute, field data.

Author contributions

J B, Y K, S C and T P performed the analyses. RBM wrote the initial draft. All authors contributed with ideas to the analyses and with writing the article. The authors declare no conflict of interest.

References

Asner G P, Townsend A R and Braswell B H 2000 Satellite observation of El Nino effects on Amazon forest phenology and productivity *Geophys. Res. Lett.* **27** 981–4

Brando P M, Goetz S J, Baccini A, Nepstad D C, Beck P S and Christman M C 2010 Seasonal and interannual variability of climate and vegetation indices across the Amazon *Proc. Natl Acad. Sci. USA* **107** 14685–90

Borchert R, Calle Z, Strahler A H, Baertschi A, Magill R E, Broadhead J S, Kamau J, Njoroge J and Muthuri C 2015 Insolation and photoperiodic control of tree development near the equator *New Phytol.* **205** 7–13

Carswell F *et al* 2002 Seasonality in CO2 and H2O flux at an eastern Amazonian rain forest *J. Geophys. Res. Atmos.* **107** LBA43–1

Chave J *et al* 2010 Regional and seasonal patterns of litterfall in tropical South America *Biogeosciences* **7** 43–55

Costa M H *et al* 2010 Atmospheric versus vegetation controls of Amazonian tropical rain forest evapotranspiration: are the

wet and seasonally dry rain forests any different? *J. Geophys. Res. Biogeosci.* **115** G04021

Da Rocha H R, Goulden M L, Miller S D, Menton M C, Pinto L D, De Freitas H C and Silva Figueira A M E 2004 Seasonality of water and heat fluxes over a tropical forest in eastern Amazonia *Ecol. Appl.* **14** S22–32

Diner D J, Asner G P, Davies R, Knyazikhin Y, Muller J P, Nolin A W, Pinty B, Schaaf C B and Stroeve J 1999 New directions in earth observing: scientific applications of multiangle remote sensing *Bull. Am. Meteorol. Soc.* **80** 2209–28

Doughty C E and Goulden M L 2008 Seasonal patterns of tropical forest leaf area index and CO_2 exchange *J. Geophys. Res. Biogeosci.* **113** G00B06

Galvão L S, Dos Santos J R, Roberts D A, Breunig F M, Toomey M and De Moura Y M 2011 On intra-annual EVI variability in the dry season of tropical forest: a case study with MODIS and hyperspectral data *Remote Sens. Environ.* **115** 2350–9

Gatti L *et al* 2014 Drought sensitivity of Amazonian carbon balance revealed by atmospheric measurements *Nature* **506** 76–80

Goulden M L, Miller S D, Da Rocha H R, Menton M C, De Freitas H C, Silva Figueira A M E and De Sousa C D 2004 Diel and seasonal patterns of tropical forest CO_2 exchange *Ecol. Appl.* **14** S42–54

Guan K *et al* 2015 Photosynthetic seasonality of global tropical forests constrained by hydroclimate *Nature Geosci.* **8** 284–9

Hasler N and Avissar R 2007 What controls evapotranspiration in the Amazon basin? *J. Hydrometeorol.* **8** 380–95

Hilker T *et al* 2014 Vegetation dynamics and rainfall sensitivity of the Amazon *Proc. Natl Acad. Sci. USA* **111** 16041–6

Huete A R *et al* 2006 Amazon rainforests green-up with sunlight in dry season *Geophys. Res. Lett.* **33** L06405

Hutyra L R *et al* 2007 Seasonal controls on the exchange of carbon and water in an Amazonian rain forest *J. Geophys. Res. Biogeosci.* **112** G03008

Jones M O, Kimball J S and Nemani R R 2014 Asynchronous Amazon forest canopy phenology indicates adaptation to both water and light availability *Environ. Res. Lett.* **9** 124021

Knyazikhin Y *et al* 1999 MODIS leaf area index (LAI) and fraction of photosynthetically active radiation absorbed by vegetation (FPAR) product (MOD15) *Algorithm Theoretical Basis Document* (https://lpdaac.usgs.gov/products/modis_products_table/mcd15a2)

Knyazikhin Y, Martonchik J, Myneni R, Diner D and Running S 1998 Synergistic algorithm for estimating vegetation canopy leaf area index and fraction of absorbed photosynthetically active radiation from MODIS and MISR data *J. Geophys. Res. Atmos.* **103** 32257–75

Knyazikhin Y, Marshak A and Myneni R B 2005 Three-dimensional radiative transfer in vegetation canopies and cloud-vegetation interaction *Three Dimensional Radiative Transfer in the Cloudy Atmosphere* ed A Marshak and A B Davis (Berlin, Heidelberg: Springer) pp 617–51

Lyapustin A I *et al* 2012 Multi-angle implementation of atmospheric correction for MODIS (MAIAC): 3. Atmospheric correction *Remote Sens. Environ.* **127** 385–93

Maeda E E, Heiskanen J, Aragão L E O C and Rinne J 2014 Can MODIS EVI monitor ecosystem productivity in the Amazon rainforest? *Geophys. Res. Lett.* **41** 7176–83

Malhado A, Costa M H, de Lima F Z, Portilho K C and Figueiredo D N 2009 Seasonal leaf dynamics in an Amazonian tropical forest *For. Ecol. Manage.* **258** 1161–5

Morton D C *et al* 2014 Amazon forests maintain consistent canopy structure and greenness during the dry season *Nature* **506** 221–4

Myneni R B *et al* 2007 Large seasonal swings in leaf area of Amazon rainforests *Proc. Natl Acad. Sci. USA* **104** 4820–3

Negrón Juárez R I, da Rocha H R, Goulden M L and Miller S D 2009 An improved estimate of leaf area index based on the histogram analysis of hemispherical photographs *Agric. For. Meteorol.* **149** 920–8

Nepstad D C *et al* 1994 The role of deep roots in the hydrological and carbon cycles of Amazonian forests and pastures *Nature* **372** 666–9

Oliveira R S, Dawson T E, Burgess S S and Nepstad D C 2005 Hydraulic redistribution in three Amazonian trees *Oecologia* **145** 354–63

Restrepo-Coupe N *et al* 2013 What drives the seasonality of photosynthesis across the Amazon basin? A cross-site analysis of eddy flux tower measurements from the Brasil flux network *Agric. For. Meteorol.* **182** 128–44

Rice A H *et al* 2004 Carbon balance and vegetation dynamics in an old-growth Amazonian forest *Ecol. Appl.* **14** 55–71

Saleska S R *et al* 2003 Carbon in Amazon forests: unexpected seasonal fluxes and disturbance-induced losses *Science* **302** 1554–7

Samanta A *et al* 2012 Seasonal changes in leaf area of Amazon forests from leaf flushing and abscission *J. Geophys. Res. Biogeosci.* **117** G01015

Wright S J and Van Schaik C P 1994 Light and the phenology of tropical trees *Am. Nat.* **143** 192–9

Xiao X *et al* 2005 Satellite-based modeling of gross primary production in a seasonally moist tropical evergreen forest *Remote Sens. Environ.* **94** 105–22

Yang W *et al* 2006 MODIS leaf area index products: from validation to algorithm improvement *IEEE Trans. Geosci. Remote Sens.* **44** 1885–98

SUPPLEMENTARY INFORMATION

Sunlight mediated seasonality in canopy structure and photosynthetic activity of Amazonian rainforests

Jian Bi, Yuri Knyazikhin, Sungho Choi, Taejin Park, Jonathan Barichivich, Philippe Ciais, Rong Fu, Sangram Ganguly, Forrest Hall, Thomas Hilker, Alfredo Huete, Matthew Jones, John Kimball, Alexei I. Lyapustin, Matti Mõttus, Ramakrishna R. Nemani, Shilong Piao, Benjamin Poulter, Scott R. Saleska, Sassan S. Saatchi, Liang Xu, Liming Zhou, and Ranga B. Myneni

This document provides Supplementary information not provided in the main text of the article "Sunlight Mediated Seasonality in Canopy Structure and Photosynthetic Activity of Amazonian Rainforests." It contains (*i*) Supplementary Data and Methods, which provides an extended description of the data and methods used; (*ii*) Supplementary Discussion related to various issues in previous studies that led to incorrect conclusions; (*iii*) Supplementary References; (*iv*) Supplementary Figures and (*v*) Supplementary Tables.

Supplementary Data and Methods

1. Study region and greening pixels
This study is focused on a 1200×1200 km² region in central Amazonia (MODIS tile "h11v09"; 0° to 10°S and 60°W to 70°W; figure S1(a)). About 95% of this region is covered with terra firme rainforests (Nepstad *et al* 1994). The average annual rainfall varies from about 1800 mm in the south to about 3700 mm in the northwest (figure S1(b)). The number of dry months, generally defined as months with rainfall less than 100 mm, varies from about 4 in the south to less than 2 in the northwest. For comparison purposes (Morton *et al* 2014), the dry season is defined as June to October (137 mm/month) and the wet season as November to May (276 mm/month). This is one of two tiles studied by (Morton *et al* 2014). Expanding the area to match that study did not alter our results and conclusions.

Terra MODIS and MISR data analysed in this study consisted of seven seasonal cycles (June to May), while the Aqua MODIS data consisted of four cycles, as in (Morton *et al* 2014). Forest pixels with valid Enhanced Vegetation Index (EVI) data are classified as greening pixels during a seasonal cycle if the average EVI value during the month of October is greater than the average EVI value during the month of June. Here, EVI refers to Terra MODIS Collection 5 EVI data (Section 2.5). The MODIS and MISR analyses in this study are focused on these "greening pixels" because we wish to address this key question: is the dry season greening purely an artefact of variations in sun-sensor geometry (Galvão *et al* 2011, Morton *et al* 2014) or does it reflect actual changes in canopy after accounting for variations in sun-sensor geometry (Xiao *et al* 2005, Huete *et al* 2006, Myneni *et al* 2007, Brando *et al* 2010, Samanta *et al* 2012)? The proportion of greening pixels varies from year to year. It averages ~60% of all rainforest pixels in the case of the Terra MODIS sensor (table S1) due to strict quality filtering. Nearly every rainforest pixel in the study region exhibits dry season greening at least once, if not more, because the data are accumulated, not averaged, over multiple seasonal cycles.

2. Data
2.1. TRMM Precipitation Data: Monthly precipitation data from the Tropical Rainfall Measuring Mission (TRMM) at quarter degree spatial resolution for the period January 1998 to December 2012 (TRMM product 3B43, Version 7) are used in this study (WWW-TRMM).
2.2. CERES Surface PAR Fluxes: Monthly at-surface Photosynthetically Active Radiation (PAR,

400-700 nm; the sum of "Computed PAR Surface Flux Direct – All-sky" and "Computed PAR Surface Flux Diffuse – All-sky") data at 1°×1° spatial resolution from June 2000 to May 2008 are used in this study (WWW-CERES).

2.3. CRU Temperature Data: The latest version of the 0.5° temperature data set produced by the Climatic Research Unit (CRU; University of East Anglia; CRU TS3.21) is used in this study (WWW-CRU).

2.4. MODIS Land Cover: Evergreen broadleaf forests in the study region are identified using the Collection 5 land cover data set "MODIS Land Cover Type Yearly L3 Global 500 m SIN Grid" (MCD12Q1) (WWW-MCD12Q1).

2.5. MODIS NIR Reflectance and EVI: The following Collection 5 EVI data are used in this study: (a) Terra Moderate Resolution Imaging Spectroradiometer (MODIS) EVI data from June 2000 to May 2008 (WWW-MOD13A2) and (b) Aqua MODIS EVI data from June 2003 to May 2008 (WWW-MYD13A2). Data from June 2005 to May 2006 are not used due to the dry season drought in 2005 (Samanta et al 2010a). These data sets also include surface reflectance at the near infrared (NIR) spectral band (858 nm) and sun-sensor measurement geometry. The data are at a spatial resolution of 1×1 km^2 and 16-day temporal frequency. The same EVI data were used in previous studies (Galvão et al 2011, Morton et al 2014). The quality of NIR reflectance and MODIS EVI data in each pixel is assessed using the 16-bit quality flags (Samanta et al 2010b, Xu et al 2011). The number of pixels with valid EVI data in June, October and March are shown in table S2.

2.6. MODIS MAIAC EVI: EVI data from Terra (June 2000 to May 2008) and Aqua (June 2003 to May 2008) MODIS sensors at 1×1 km^2 spatial resolution and 8-day temporal frequency generated with the Multi-angle Implementation of Atmospheric Correction (MAIAC) algorithm (Lyapustin et al 2012) are used in this study (WWW-MAIAC). The MAIAC EVI data are standardized to a fixed sun-sensor geometry (nadir viewing direction, solar zenith angle of 45°). Thus, the MAIAC EVI data are free of sun-sensor geometry effects.

2.7. MODIS LAI: Collection 5 Leaf Area Index (LAI) data from Terra MODIS for the period June 2000 to May 2008 are used in this study (WWW-MOD15A2). Data from June 2005 to May 2006 are excluded from analyses of LAI seasonal changes (figures 1 and 2) due to the dry season drought in 2005 (Samanta et al 2010a). The data are at 1×1 km^2 spatial resolution and 8-day temporal frequency. Valid LAI data in each 1×1 km^2 8-day pixel are identified using quality flags (Samanta et al 2011, Poulter and Cramer, 2009).

2.8. MISR Bidirectional Reflectance Factor: Land Surface Data (version 22) from the Terra Multiangle Imaging Spectroradiometer (MISR) for the period June 2000 to May 2008 are used in this study (WWW-ASDC). Data from June 2005 to May 2006 are not used due to the dry season drought in 2005 (Samanta et al 2010a). The data are at a spatial resolution of 1.1 × 1.1 km^2 and include Bidirectional Reflectance Factors (BRF) at the nine MISR view angles (nadir, $\pm 26.1°$, $\pm 45.6°$, $\pm 60.0°$ and $\pm 70.5°$) in four spectral bands (446, 558, 672, and 866 nm). MISR data with LandQA=0 (cloud free, aerosol optical depth below 0.3) are considered valid.

2.9. GLAS Centroid and Apparent Reflectance: Data from the Geoscience Laser Altimeter System (GLAS) instrument onboard the Ice, Cloud and land Elevation Satellite (ICESat) acquired during four periods – May 20 to June 23, 2005 (L3c), May 24 to June 26, 2006 (L3f), October 3 to November 8, 2004 (L3a) and October 2 to November 5, 2007 (L3i) – are used to analyze the sensitivity of the waveform centroid relative height (WCRH) and Apparent Reflectance (AR) to LAI (WWW-GLAS). The same data were used in (Morton et al 2014). For comparison purposes, low quality data were filtered as described in (Morton et al 2014). Additionally, GLAS footprints over non-forest and/or bare ground were screened by imposing the following conditions: (a) MODIS Land Cover corresponding to GLAS footprints is "Evergreen Broadleaf Forests" and (b) number of GLAS waveform Gaussian peaks exceeds one. GLAS lidar analysis is focused on the region spanning 0° to 10°S and 60°W to 80°W – the spatial extent of the blue and red squares in figure S1(a).

3. Sun-Sensor Geometry
Three angles characterize the sun-sensor geometry of a pixel (figure S1(c)): (a) solar zenith angle (SZA), (b) relative azimuth angle (RAA), and (c) view zenith angle (VZA). All three change

during the year in the case of MODIS. The distribution of these angles for pixels in the study region during each of the twenty-three 16-day compositing periods in a year is shown in figure 1 for Terra MODIS. The geometry for Aqua MODIS is very similar to that of Terra MODIS. The view zenith angles are fixed in the case of MISR. The following discussion of sun-sensor geometry is specific to this study's region (figure S1(a)).

The geometry in terms of SZA and RAA is approximately cyclical with a period of six months (figures 1(b) and (c)). Terra and Aqua MODIS and Terra MISR measurements are made at higher SZA ($\sim 30^o$ to 40°) about the solstices, June/July and December/January, and at lower SZA ($\sim 20^o$ to 30°) about the equinoxes, September/October and February/March (figure 1(b)). The progression of Terra and Aqua MODIS RAA during the year shows a similar cyclical behavior (figure 1(c)). The measurements are made closer to the solar azimuthal plane, or the principal plane, (RAA $\sim 0°$ and $180°$), about the equinoxes and approximately $\pm30°$ to $\pm45°$ off the orthogonal plane (RAA $\sim 130^o$ and 50°) about the solstices (figure 1(c) and figure S2). View zenith angle varies between $0°$ (nadir) and $60°$ (figure 1(d)). The RAA of MISR sampling along the spacecraft flight track follows its Terra counterpart, but is shifted by about $90°$ (not shown). Half of Terra and Aqua MODIS observations about the solstices were collected at VZA below $15°$ and $20°$, respectively. Around 50% of the measurements about the equinoxes were made at VZA below $35°$ (Terra) and $20°$ (Aqua). The MISR VZAs are strongly peaked as expected around their nominal values of $0.0°$, $\pm26.1°$, $\pm45.6°$, $\pm60.0°$ and $\pm70.5°$ (figure S2).

Choosing three 16-day composites, one each in June (Jun 25 to Jul 10), October (Oct 15 to 30) and March (Mar 5 to 20), is sufficient to assess whether the previously reported seasonality in radiometric greenness (Xiao *et al* 2005, Huete *et al* 2006, Brando *et al* 2010) and leaf area (Myneni *et al* 2007, Samanta *et al* 2012) of Amazonian rainforests is an artefact of sun-sensor geometry (Galvão *et al* 2011, Morton *et al* 2014) or not. The three periods correspond to the beginning of the dry season, end of the dry season and mid wet season, respectively. The Terra and Aqua MODIS observations provide pairs of matching RAA (October vs. March), varying RAA (June vs.

October), matching SZA (Terra and Aqua in June and March), varying SZA (October from Terra and Aqua) (figure S2). The Terra MISR sensor samples the surface close to the principal plane in June and near the orthogonal plane in October and March. This manner of sampling is opposite to that of MODIS (figure S2). The juxtaposition of MODIS and MISR sampling provides an interesting opportunity for assessing the presence or absence of seasonal variations in these rainforests.

4. Forest Reflectance

4.1. Bidirectional Reflectance Factor (BRF):
The reflected radiation field from a vegetation canopy illuminated by a solar beam in a coordinate system with the polar axis pointed to the sun is considered here. The reflected radiance is expressed relative to a surface perpendicular to the solar beam and depends on the phase angle, γ, and azimuth, ψ. The phase angle is the angle between the directions to the sun and sensor (figure S1(c)). The plane ψ is chosen such that the phase angle varies between $-(90° + \theta_0)$ and $+(90° - \theta_0)$ where θ_0 is the sun zenith angle. In this coordinate system the Bidirectional Reflectance Factor, $BRF(\gamma, \psi)$, is the ratio of radiance reflected from the vegetation canopy to the radiance reflected from an ideal Lambertian surface under identical illumination conditions. The Lambertian surface in this instance is perpendicular to the solar beams. For a plane given by ψ and $\psi + 180°$, the BRF is a function of SZA, phase angle and wavelength. Its magnitude and angular shape depends on the composition, density, geometric structure of the reflecting medium, in addition to the foliage optical properties.

4.2. Transformation of MODIS and MISR BRF data:
Let $BRF_{xy}(\theta_0, \theta_v, \Delta\varphi)$ be the observed BRF at a location (x, y) on the Earth's surface. The BRF_{xy} is a standard product of MODIS and MISR sensors, which is expressed relative to a horizontal surface. The sun-sensor geometry is represented by the sun, θ_0, and sensor, θ_v, view zenith angles, and the view azimuth φ_v (figure S1(c)). First, we introduce a new coordinate system with the polar axis pointed to the sun. The quantities, $I_{xy} = BRF_{xy} \cos\theta_0$, represent radiances reflected from forests illuminated by a

parallel beam of unit intensity. The radiances are expressed relative to the unit surface perpendicular to the solar beam and depend on the phase angle, γ, and azimuth, ψ, in this system. The phase angle is the angle between directions to the sun and sensor, i.e., $\gamma = \text{acos}[\cos\theta_v \cos\theta_0 + \sin\theta_v \sin\theta_0 \cos\varphi_v]$.

Second, we group I_{xy} with respect to the phase angle (figure S3). This procedure transforms the standard BRF product into BRF expressed in terms of the phase angle, γ, and azimuth, ψ. The azimuth specifies sampling plane of satellite-borne sensors. The MODIS instrument scans the Earth across the Terra and Aqua spacecraft flight track, which is approximately from East to West (figure S3(a)). The MISR instrument measures reflected radiation along the Terra flight track, which is approximately from North to South (figure S3(b)). The sampling planes are fixed for MODIS and MISR instruments. We assign the sign "plus" to γ if the direction to the sensor approaches the direction to sun from East (Terra MODIS), West (Aqua MODIS) or North (Terra MISR), and "minus" otherwise. The phase angle varies between $-(90° + \theta_0)$ and $90° - \theta_0$. The probability density distribution function $p(\theta_0, \gamma)$ of the phase angle is evaluated from the fraction of data in each group.

Finally, the reflected radiances in each group are averaged. This methodology is applied to transform standard BRF products from Terra and Aqua MODIS observations (figure S3(a)). In the case of MISR, the algorithm is applied to each MISR camera to derive camera specific BRF (figure S3(b)) and corresponding probability density functions. The camera specific BRFs for which $|\gamma - \bar{\gamma}| \leq \sigma$ are used in further analyses. Here $\bar{\gamma}$ and σ denote camera specific mean and standard deviation of the phase angle γ.

4.3. Effect of Changing Canopy Properties on BRF: figures S5(a) and (b) illustrate the effect of changing canopy properties on BRF. Here, SZA is held constant. An increase in LAI, with leaf optical properties unchanged, increases the interception of incoming solar radiation by the vegetation canopy, which in turn increases the amount of reflected radiation. This increases the magnitude of BRF at all phase angles, i.e. a non-linear upward shift in the angular signature of the BRF, as shown in figure S5(b). The overall shape of the BRF remains unchanged. This is a well-known fact: the reflectance of dense vegetation, or a vegetation canopy with a dark background, is an increasing function of LAI (e.g. figure 1 in (Huang et al 2008)). Changes in leaf optical properties either augment or suppress the LAI effect on the reflectance factor (Samanta et al 2012). Thus, changing canopy properties and holding SZA constant changes the magnitude of the BRF but not the overall shape of the signature. This explains the observed BRF changes in figures 3(a) and (b).

4.4. Effect of Changing SZA on BRF: figures S5(c) and (d) illustrate the effect of changing SZA on BRF. Here, canopy properties are held constant. The cumulative contribution of within-canopy sources generated by single- and multiple-scattered photons to canopy-exiting radiation along a given direction increases with photon path length, L, as $\sim(1 - \exp(-\sigma L))$, where L is the distance between sources within the canopy and the upper boundary of the canopy and σ is the extinction coefficient. An increase in SZA results in longer photon path lengths for positive phase angles (figure S5(c)). The opposite is true for negative phase angles. Increasing SZA with constant canopy therefore results in an asymmetric transformation of the BRF signature, that is, enhanced values for positive phase angles and depressed values for negative phase angles (figure S5(d)). It also decreases the range of BRF variation at positive phase angles and a corresponding increase in the range of BRF variation at negative phase angles. Thus, both the shape and magnitude of the BRF signature are changed. The asymmetric transformation also causes the two BRF signatures to intersect, as illustrated in figure S5(d). The phase angle at which the two signatures intersect can be calculated using the principle of directional reciprocity (Section 4.6).

It is important to note that the path L varies with SZA as $\sim 1/\cos(SZA)$. It means that effect of changing SZA on the BRF's angular shape is weak at low SZA. For example, a change in SZA from 20° to 30° involves a change in L from ~ 1.06 to ~ 1.15. The impact, however, increases with SZA. This explains why SZA variation has no discernable impact on the angular signatures of reflectances in figures 3(a) and (b).

4

4.5. Effect of Changing Canopy Properties and SZA on BRF:

4.5. Effect of Changing Canopy Properties and SZA on BRF: figures S5(e) and (f) illustrate the effect of changing both canopy properties and SZA on BRF. Changing canopy properties but holding SZA constant changes the magnitude of BRF but retains its overall angular shape (Section 4.3). Changing SZA but holding canopy properties invariant changes the magnitude of BRF differently for positive and negative phase angles, thus changing the shape of the BRF as well (Section 4.4). Changing canopy properties and SZA simultaneously combines these two effects, i.e. the BRF is transformed asymmetrically and shifted in magnitude. For example, decreasing SZA depresses the BRF at positive phase angles and enhances the same at negative phase angles – transformation of the green colored BRF signature to dashed-blue color signature in figure S5(f). Increasing canopy properties, say LAI and/or foliage optical properties, shifts the overall BRF signature up in magnitude – transformation of the dashed-blue color signature to solid-blue color signature in figure S5(f). This explains the BRF signature changes in figures 3(c) and (d). Importantly, it follows from this argumentation that *higher or equal values of BRF at lower SZA relative to BRFs at higher SZA always indicate a change in canopy properties*.

4.6. Proof of Dry Season Changes From the Directional Reciprocity Principle: The optical reciprocity theorem (Davis and Knyazikhin, 2005) provides a proof relevant to our study. It states that switching detector and source and inverting the directions of propagation yield the same result for BRF. It follows from the theorem that the BRFs of a canopy, or two similar canopies, corresponding to different sun positions, say Ω_0 and Ω_1, necessarily intersect at $\gamma_0 = -\mathrm{acos}(\Omega_0 \cdot \Omega_1)$. Indeed, the BRF in direction Ω_1 due to a mono-directional solar beam in direction $-\Omega_0$ is related to the BRF in direction Ω_0 due to a mono-directional solar beam in direction $-\Omega_1$ as $BRF(-\Omega_0, +\gamma) = BRF(-\Omega_1, -\gamma)$. If $BRF(-\Omega_0, \gamma)$ is symmetric at $\gamma_0 = \mathrm{acos}(\Omega_0 \cdot \Omega_1)$ (e.g., as in October), the BRFs should intersect at $\gamma_0 = -\mathrm{acos}(\Omega_0 \cdot \Omega_1)$. Changing canopy properties with illumination conditions unchanged results in an upward or downward shift in the angular signature of the BRF (Section 4.5). This causes the intersection point to deviate from γ_0, indicating a difference in canopy properties. The deviation of the intersection point around $-5.5°$ from $\gamma_0 = -37.1°$ shown in figure 3(d) is significant, indicating *different canopy properties in June and October*.

Supplementary Discussion

Galvão *et al* (2011) and Morton *et al* (2014) claim that previous studies (Xiao *et al* 2005, Huete *et al* 2006, Myneni *et al* 2007, Brando *et al* 2010, Samanta *et al* 2012) misinterpreted changes in near-infrared (NIR) reflectance caused by seasonal changes in sun-satellite sensor geometry as seasonal variations in rainforest canopy structure and greenness. They conclude that Amazonian rainforests maintain consistent structure and greenness during the dry season based on their analysis of satellite borne sensor data (MODIS and Lidar) and model exercises. Here we present a detailed critique of their analysis.

An incomplete analysis of the seasonal cycle, i.e. one that is focused only on the dry season, encourages misleading interpretation of both intra- and inter-annual greenness (EVI or LAI) variations as artefacts of changing sun-sensor geometry. For example, if the sun-sensor geometry artefact argument is valid, then the seasonal course of LAI from December to May should be similar to that from June to November because of a repeat in sun-sensor geometry (figures 1(b) and (c)), but it is not (figure 1(a)). Also, if the change in MODIS sampling from the orthogonal plane in June to the principal plane in October (figures S2(a) and (c)) causes the rainforests to appear greener, then the change in MISR sampling from the principal plane in June to the orthogonal plane in October (figures S2(b) and (d)) should cause the rainforests to appear browner. But, greening is observed as well (figure 3(d)).

Interannually, the attribution of anomalous dry season greening (increase in EVI or LAI) in drought year 2005, *vis a vis* dry seasons of non-drought years, to a higher proportion of brighter backscattering MODIS observations is flawed because it is selectively based on data from the first fortnight of October (ED-figure 9 (Morton *et al* 2014)). A higher fraction of backscattering measurements is not seen in 2005 when the analysis is focused on July to September period

5

(figure S4(b)) as in the original studies (Samanta *et al* 2010a, Samanta *et al* 2010b, Saleska *et al* 2007). Moreover, if claims of geometric artefacts are true, higher backscatter fraction and greenness should also be seen during the more intense dry season drought in 2010 (Xu *et al* 2011). They are not (figure S4(b)), even in their selective analysis (ED-figure 9 (Morton *et al* 2014)).

Crucially, the misinterpretations in Morton *et al* (2014) stem from reliance on prognostications of an untested radiative transfer model. In a critical test of how well the model simulates variation in sunlit and shaded proportions of the canopy, which is central to arguments about geometric artefacts, the model underestimates measurements by ~45% (figure S4(c)). The model is also unrealistically sensitive to litter reflectance in dense vegetation (table 1 (Morton *et al* 2014)), an indication of incorrect physics and/or modeling of foliage spatial distribution. The failure to test the model is compounded by an unquestioned belief in its validity, else the observed dry season greening in geometry-corrected EVI would not have been ignored (figure 3(b) (Morton *et al* 2014) and ED-figure 7(b) (Morton *et al* 2014)). Various statistical analyses of this geometry-corrected EVI data strongly reject the null hypothesis of no change in forest greenness (Saleska *et al* 2015). Indeed the physics of radiative transfer in dense media (Section 2.9 (Knyazikhin *et al* 1999)) informs that these changes in geometry-corrected EVI (figure 2, figure 3(b) in (Morton *et al* 2014) and ED-figure 7(b) in (Morton *et al* 2014)) correspond to large changes in LAI (figure. 1(a)). Thus, there is no valid statistical or theoretical basis to dismiss dry season increase in geometry-corrected EVI (figure 2(b), figure 3(b) in (Morton *et al* 2014) and ED-figure 7(b) in (Morton *et al* 2014)).

The unorthodox belief that Amazonian rainforests should conform to model predictions affects their interpretation of satellite lidar data also. The conclusion that structure and greenness of rainforests remain invariant does not follow from absence of evidence in lidar data for their model prediction that an increase in LAI from 4.5 to 6.5 should result in an increase in Waveform Centroid Relative Height - the height of median return energy relative to the full waveform extent (WCRH; table 1 in (Morton *et al* 2014)). A

prudent interpretation might be that the model prediction does not conform to data. Even if the model is assumed to be capable of accurate predictions, the predicted change in WCRH (0.06) is comparable to the spatial standard deviations of June and October WCRH data (~0.07). This clearly suggests a need for additional analysis.

The lack of insight into what might be reasonably expected from lidar data and saturation of lidar signals in dense vegetation compound the problem of detecting seasonal LAI changes. For example, studies that have investigated the relationship between LAI and lidar waveforms (Castillo *et al* 2012, Tang *et al* 2012, Drake *et al* 2002) show that WCRH saturates in mature and secondary growth tropical forests aged over ~20 years (Tang *et al* 2012, Drake *et al* 2002) because the majority of lidar hits are confined to the upper canopy. This saturation of signals emanating from vegetation is different than sensor saturation (Neuenschwander *et al* 2008) – the latter have been filtered out from all analyses.

The saturation effect can be potentially documented through these three analyses. First, although a range of LAI values are observed in Amazonian rainforests, from about 4 to 6 in June and greater than 6 in October, the two lidar metrics, WCRH and Apparent Reflectance (AR), exhibit no correspondent variations (figure S6). Second, rainforests with low (3.5 to 4.5) and high (greater than 5.5) LAI have the same WCRH and AR (figures S7 (a) and (b)). Third, rainforests with low (<0.5) and high (>0.6) WCRH have the same LAI (figure S7(c)). Likewise, rainforests with low (<0.5) and high (>0.6) AR have identical LAI (figure S7(d)). Inference of saturation from figure S6 and figures S7 (a)–(d) depends on the validity of the MODIS LAI data. To alleviate this concern, we present similar results for deciduous broadleaf forests where a broader range of LAI values are encountered. The curvilinear relationship in deciduous forests, where WCRH increases for LAI values 0 to 3 and saturates thereafter (figures S8(a) and (c)), is as expected, and is similar to other relations between LAI and remote measurements (Knyazikhin *et al* 1999, Huang *et al* 2008).

Unlike WCRH, the AR shows no relationship to LAI (figures S6 (b) and (d), figures S8 (b) and (d)), even in sparsely foliated canopies (LAI less

6

than 3; figures S8 (b) and (d)). Also, the inverse relationship with WCRH is perplexing (figures S7 (e) and (f)). To ascertain whether these results indicate potential data quality problems, we investigated the relationship between the lidar metrics and key climatic variables that govern plant growth, i.e. water, radiation and temperature (Nemani *et al* 2003). The WCRH data are positively related (p-value < 0.001) to all three climatic variables (table S4). This is as it should be, i.e. tall and dense tree stands with higher WCRH are located in climatically favorable environments of higher annual precipitation, solar radiation and mean temperature (table S4). The AR data, on the other hand, show negative relation with two of the three climatic variables. We therefore conclude that GLAS AR data have quality problems.

Morton *et al* (2014)'s interpretations of AR data are contradictory - on the one hand, their validity is discounted by citing corruption from aerosols due to biomass burning, and on the other hand, their invariance is counted as proof that Amazonian rainforests maintain consistent structure and greenness (figure 2(c) (Morton *et al* 2014)). Why table 1 (Morton *et al* 2014) does not show model predictions of AR seasonal variations, unlike WCRH, is unknown. Given these ambiguities, their analyses of AR data must also be deemed inconclusive.

In addition to the analyses presented in this article, three independent studies have rebutted Galvão *et al* (2011) and Morton *et al* (2014) claims with a multitude of satellite and in situ data (Maeda *et al* 2014, Hilker *et al* 2014, Jones *et al* 2014). Dry season greening in sun-sensor geometry corrected data obtained from Morton et al. is due for publication (Saleska *et al* 2015).

Supplementary References

Brando P M, Goetz S J, Baccini A, Nepstad D C, Beck P S and Christman M C 2010 Seasonal and interannual variability of climate and vegetation indices across the Amazon. *Proc. Natl. Acad. Sci. USA.* **107** 14685–14690

Castillo M, Rivard B, Sánchez-Azofeifa A, Calvo-Alvarado J and Dubayah R 2012 LIDAR remote sensing for secondary Tropical Dry Forest identification. *Remote Sens. Environ.* **121** 132–143

Davis A B and Knyazikhin Y 2005 A primer in 3D radiative transfer. *Three Dimensional Radiative Transfer in the Cloudy Atmosphere*, eds Marshak A, Davis A B (Springer-Verlag, Berlin Heidelberg), pp 153-242

Drake J B, et al. 2002 Estimation of tropical forest structural characteristics using large-footprint lidar. *Remote Sens. Environ.* **79** 305–319

Galvão L S, Dos Santos J R, Roberts D A, Breunig F M, Toomey M and de Moura Y M 2011 On intra-annual EVI variability in the dry season of tropical forest: A case study with MODIS and hyperspectral data. *Remote Sens. Environ.* **115** 2350–2359

Hilker T *et al* 2014 Vegetation dynamics and rainfall sensitivity of the Amazon. *Proc. Natl. Acad. Sci. USA.* **111** 16041–16046

Huang D *et al* 2008 Stochastic transport theory for investigating the three-dimensional canopy structure from space measurements. *Remote Sens. Environ.* **112** 35–50

Huete A R *et al* 2006 Amazon rainforests green-up with sunlight in dry season. *Geophys. Res. Lett.* **33** L06405

Jones M O, Kimball J S and Nemani R R 2014 Asynchronous Amazon forest canopy phenology indicates adaptation to both water and light availability. *Environ. Res. Lett.* **9** 124021

Knyazikhin Y *et al* 1999 *MODIS leaf area index (LAI) and fraction of photosynthetically active radiation absorbed by vegetation (FPAR) product (MOD15) algorithm theoretical basis document*, <https://lpdaac.usgs.gov/products/modis_products_table/mcd15a2>

Lyapustin A I *et al* 2012 Multi-angle implementation of atmospheric correction for MODIS (MAIAC): 3. Atmospheric correction. *Remote Sens. Environ.* **127** 385–393

Maeda E E, Heiskanen J, Aragão L E O C and Rinne J 2014 Can MODIS EVI monitor ecosystem productivity in the Amazon rainforest? *Geophys. Res. Lett.* **41** 7176–7183

Morton D C *et al* 2014 Amazon forests maintain consistent canopy structure and greenness during the dry season. *Nature* **506** 221–224

Myneni R B *et al* 2007 Large seasonal swings in leaf area of Amazon rainforests. *Proc. Natl. Acad. Sci. USA* **104** 4820–4823

Nemani R R *et al* 2003 Climate-driven increases in global terrestrial net primary production from 1982 to 1999. *Science* **300** 1560–1563

Nepstad D C *et al* 1994 The role of deep roots in the hydrological and carbon cycles of Amazonian forests and pastures *Nature* **372** 666–669

Neuenschwander A L, Urban T J, Gutierrez R and Schutz B E 2008 Characterization of ICESat/GLAS waveforms over terrestrial ecosystems: Implications for vegetation mapping. *J. Geophys. Res. Biogeosci.* **113** G02S03

Poulter B and Cramer W 2009 Satellite remote sensing of tropical forest canopies and their seasonal dynamics. *Int. J. Remote Sens.* **30** 6575–6590

Saleska S R *et al* 2015 Dry-season greening of Amazon forests. Brief Communications Arising in *Nature* (in press)

Saleska S R, Didan K, Huete A R and Da Rocha H R 2007 Amazon forests green-up during 2005 drought. *Science* **318** 612–612

Samanta A *et al* 2010a Amazon forests did not green-up during the 2005 drought. *Geophy. Res. Lett.* **37** L05401

Samanta A *et al* 2012 Seasonal changes in leaf area of Amazon forests from leaf flushing and abscission. *J. Geophys. Res. Biogeosci.* **117** G01015

Samanta A, Costa M H, Nunes, E L, Vieira S A, Xu, L and Myneni R B 2011 Comment on "Drought-Induced Reduction in Global Terrestrial Net Primary Production from 2000 Through 2009". *Science* **333** 1093

Samanta A, Ganguly S and Myneni R B 2010b MODIS Enhanced Vegetation Index data do not show greening of Amazon forests during the 2005 drought. *New Phytol.* **189** 11–15

Tang H *et al* 2012 Retrieval of vertical LAI profiles over tropical rain forests using waveform lidar at La Selva, Costa Rica. *Remote Sens. Environ.* **124** 242–250

WWW-ASDC. NASA Langley Research Center Atmospheric Science Data Center (ASDC) Home page. Available at https://eosweb.larc.nasa.gov/

WWW-CERES. Atmospheric Science Data Center: The Clouds and the Earth's Radiant Energy System (CERES). Available at https://eosweb.larc.nasa.gov/project/ceres/ceres_table

WWW-CRU. Climatic Research Unit (CRU) Time-Series High-Resolution Gridded Datasets. Available at http://www.cru.uea.ac.uk/cru/data/hrg/

WWW-GLAS. Geoscience Laser Altimeter System (GLAS) lidar waveform data. Available at https://nsidc.org/data/icesat/data-dictionaries-landing-page.html

WWW-MAIAC. MAIAC Amazon Data. *Level 1 and Atmosphere Archive and Distribution System (LAADS)*. Available at ftp://ladsweb.nascom.nasa.gov/MAIAC/

WWW-MCD12Q1. Land Cover Type Yearly L3 Global 500 m SIN Grid (MCD12Q1). *Land Process Distributed Active Archive Center*. Available at https://lpdaac.usgs.gov/products/modis_products_table/mcd12q1

WWW-MOD13A2. Vegetation Indices 16-Day L3 Global 1km (MOD13A2). *Land Process Distributed Active Archive Center*. Available at https://lpdaac.usgs.gov/products/modis_products_table/myd13a12

WWW-MOD15A2. Leaf Area Index - Fraction of Photosynthetically Active Radiation 8-Day L4 Global 1km (MOD15A2). *Land Process Distributed Active Archive Center.* Available at https://lpdaac.usgs.gov/products/modis_products_table/mod15a12

WWW-MYD13A2. Vegetation Indices 16-Day L3 Global 1km (MYD13A2). *Land Process Distributed Active Archive Center*. Available at https://lpdaac.usgs.gov/products/modis_products_table/myd13a12

WWW-TRMM. Tropical Rainfall Measuring Mission (TRMM) data. *Goddard Earth Science Data and Information Center*. Available at http://mirador.gsfc.nasa.gov/

Xiao X *et al* 2005 Satellite-based modeling of gross primary production in a seasonally moist tropical evergreen forest. *Remote. Sens. Environ.* **94** 105–122

Xu L *et al* 2011 Widespread decline in greenness of Amazonian vegetation due to the 2010 drought. *Geophy. Res. Lett.* **38** L07402

Yang W *et al* 2006 MODIS leaf area index products: From validation to algorithm improvement. *IEEE Trans. Geosci. Remote. Sens.* **44** 1885–1898

Supplementary Figures
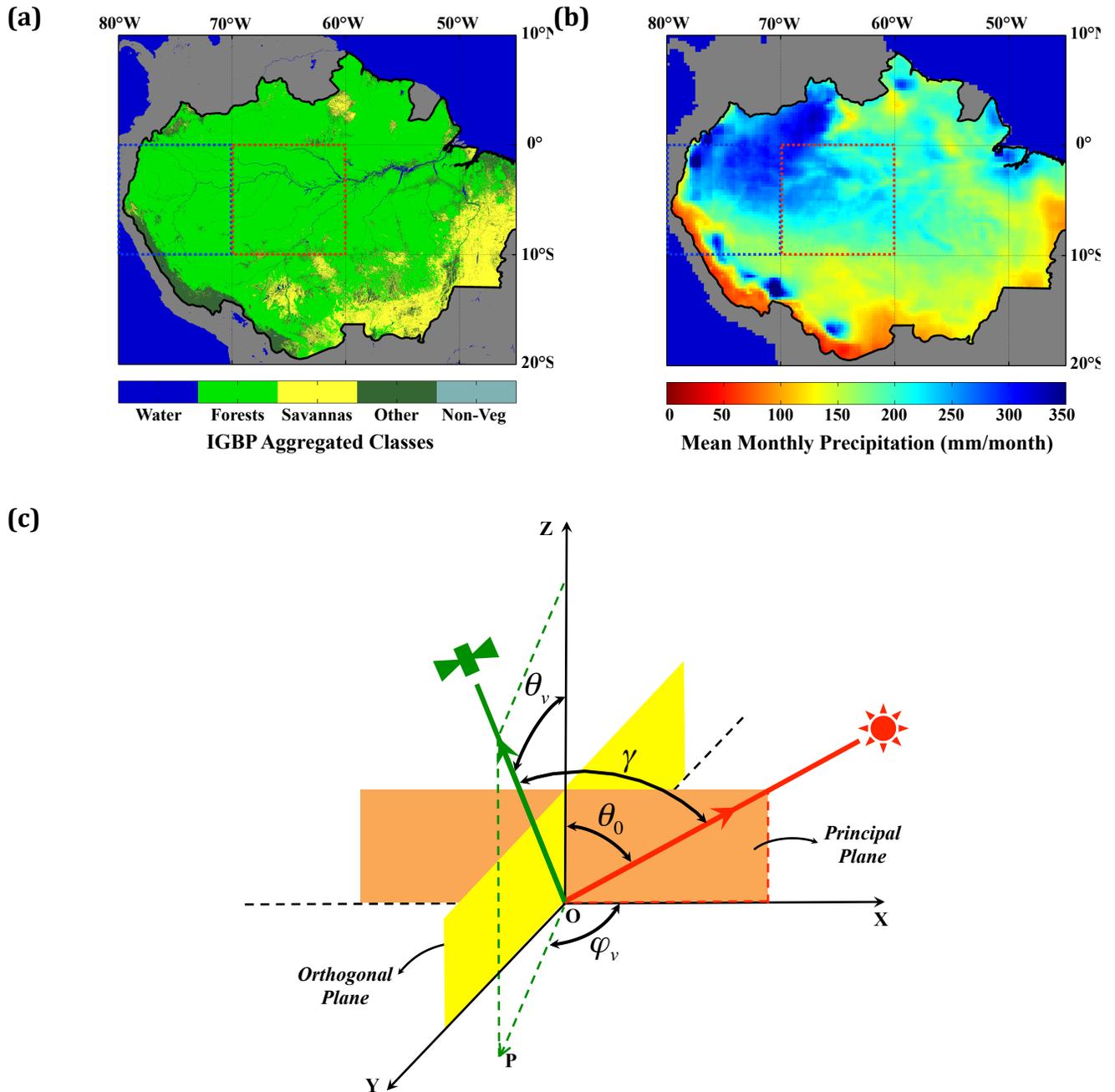
(a)

(b)

(c)

Figure S1. The study domain and sun-sensor geometry. (a) The domain of MODIS and MISR analysis is the red square. The domain of GLAS lidar analysis is both blue and red squares. (b) Monthly mean rainfall from TRMM. (c) Three angles characterize the sun-sensor measurement geometry of a pixel: (1) solar zenith angle, SZA=θ_0 ($0° < \theta_0 \leq 90°$), (2) view zenith angle, VZA=θ_v ($0° \leq \theta_v \leq 90°$) and (3) view azimuth, φ_v ($0° \leq \varphi_v \leq 360°$), measured relative to the principal plane. The angle between the projection, OP, of the direction to the sensor and X axis is the relative azimuth angle (RAA), i.e., RAA=φ_v if $0 \leq \varphi_v < 180°$ and RAA=$360° - \varphi_v$, otherwise. It varies between 0° and 180°. The angle between the directions to the sun and sensor is the phase angle, PA=γ.

9

(a)

(b)

(c)
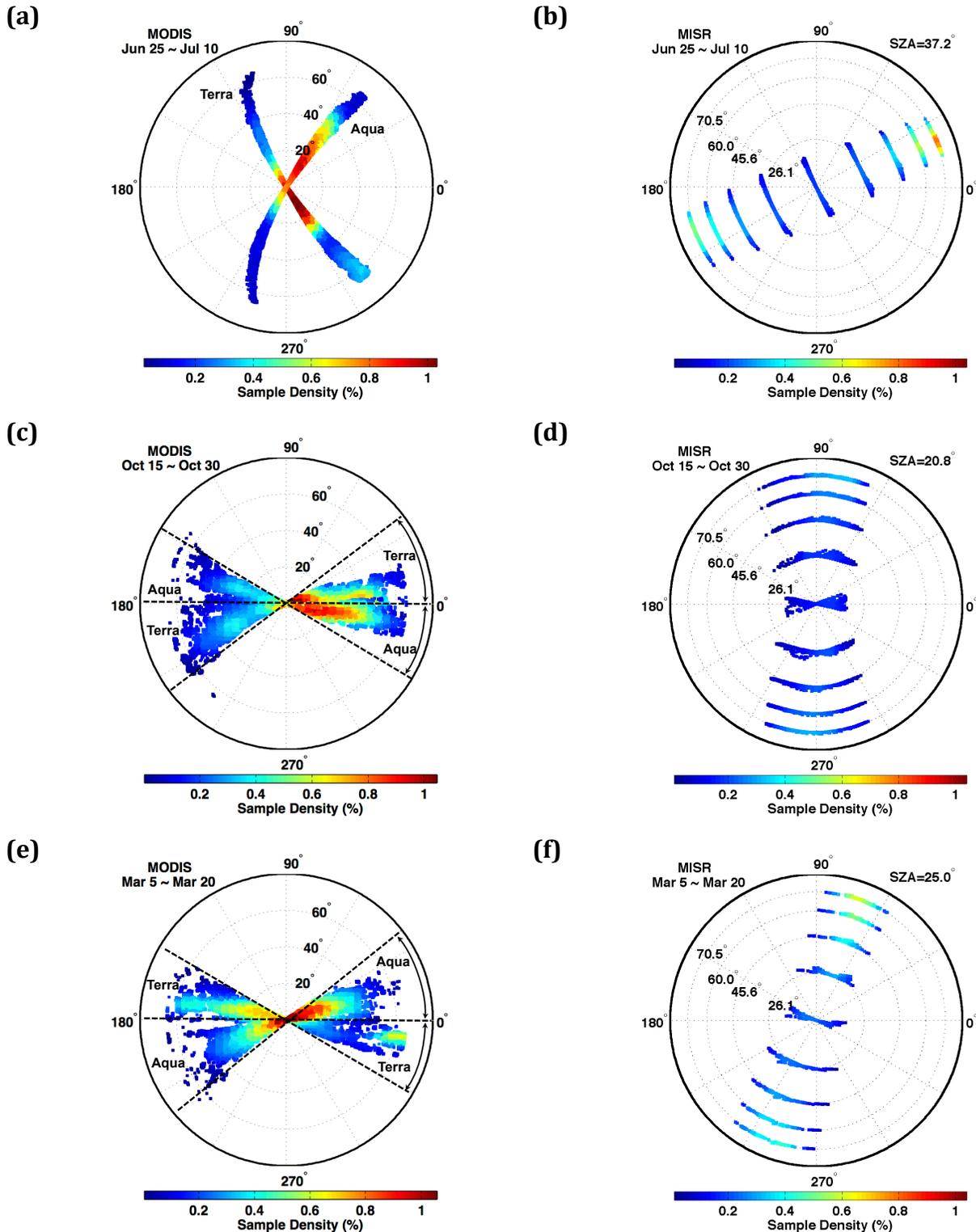
(d)

(e)

(f)

Figure S2. MODIS and MISR sampling geometries. Terra and Aqua MODIS (left panels) and Terra MISR (right panels) sampling geometries during a 16-day compositing period in the months of (a, b) June 2003, (c, d) October 2003, and (e, f) March 2003. The MODIS sensors sample the surface close to the orthogonal plane in June and near the principal plane in October and March. This sampling is opposite to that of MISR sensor.
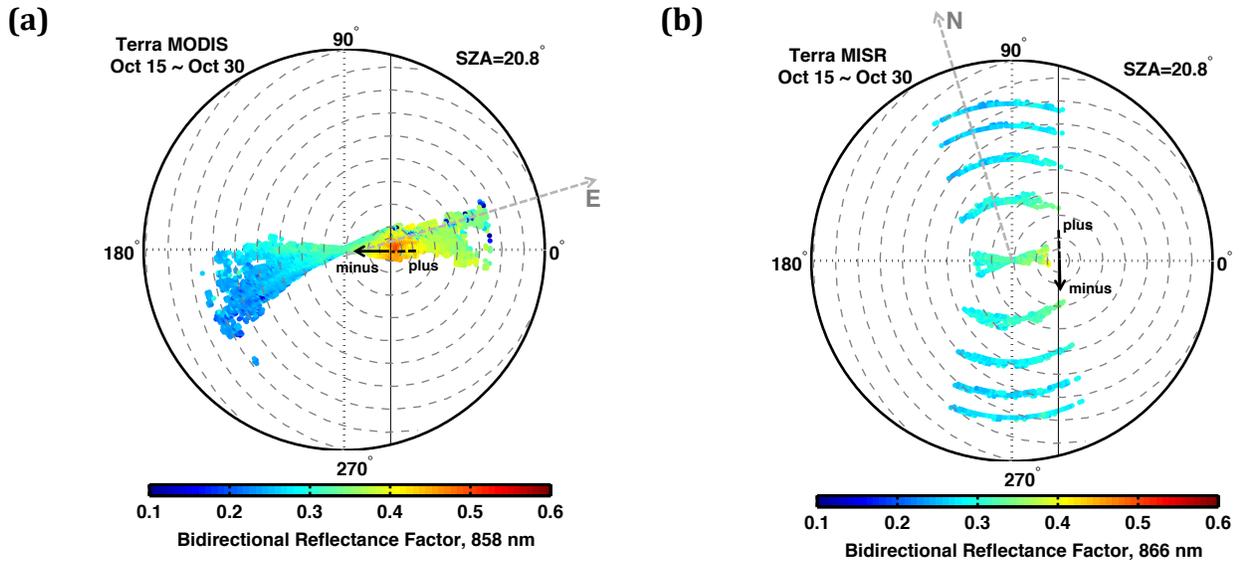
Figure S3. MODIS and MISR reflectances in a modified coordinate system. Terra MODIS (a) and MISR (b) NIR BRFs during a 16-day composite in October 2003. BRF values are expressed in a coordinate system with the polar axis pointed to the Sun. Solid arrows indicate sampling direction that determines the phase angle sign (angle between solar and sensor view directions).
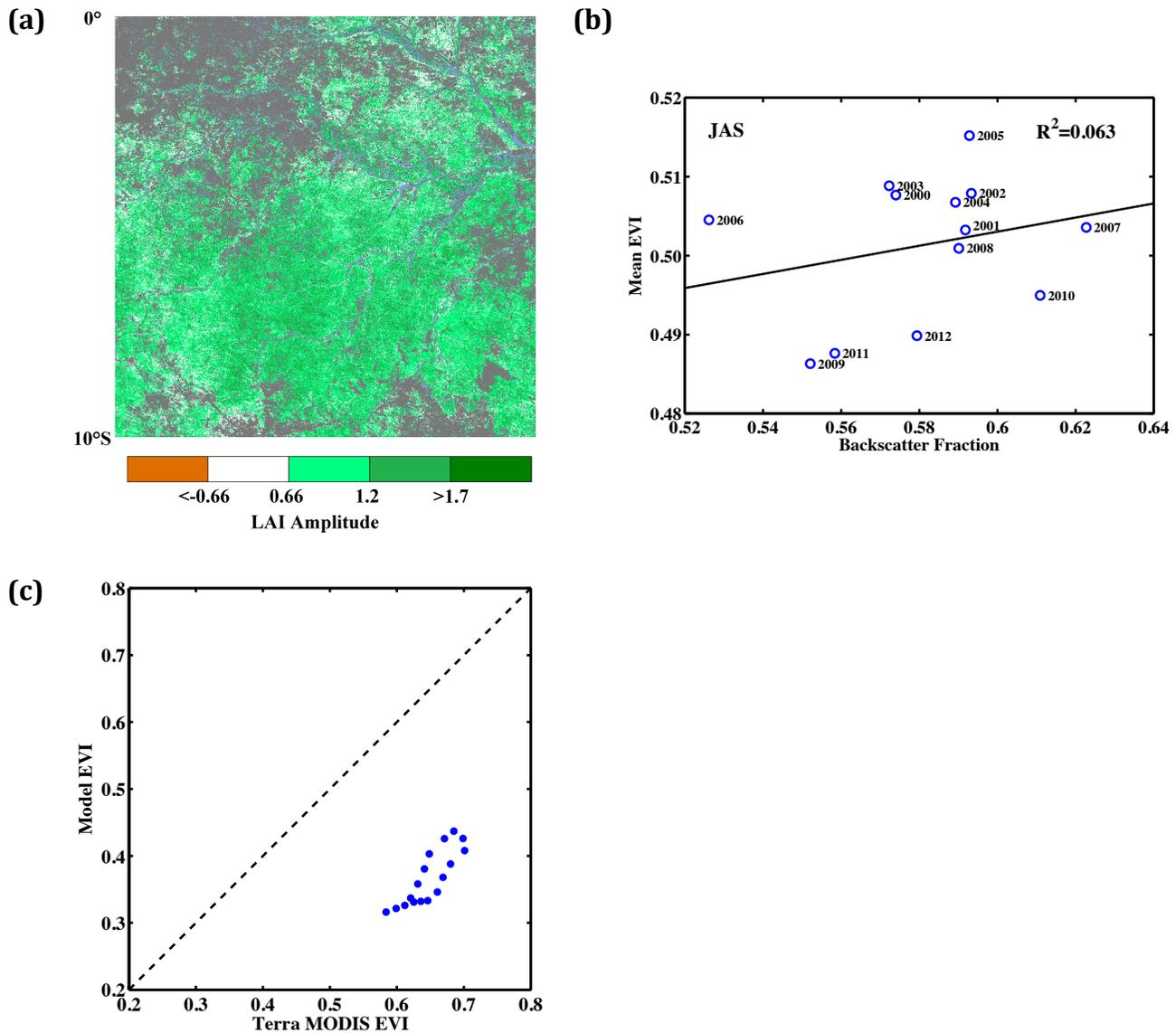
(a)

0°

10°S

<-0.66   0.66   1.2   >1.7

LAI Amplitude

(b)

JAS   R²=0.063

2005

2003
2000
2004   2002
2006   2001
2008

2007

2010

2012

2011
2009

Mean EVI

Backscatter Fraction

(c)

Model EVI

Terra MODIS EVI

Figure S4. Evidence for seasonality of leaf area and misinterpretation of data following the guidance of an erroneous radiative transfer model (Morton *et al* 2014). (a) Spatial pattern of seasonal Terra MODIS LAI amplitude expressed as the difference between the maximum value during September to November and the minimum value during the following May to June period. White pixels denote locations with LAI amplitudes less than |0.66|, which is the accuracy of MODIS LAI data (Yang *et al* 2006). White and colored pixels together denote pixels that exhibited dry season greening in at least 4 out of 7 seasonal cycles (63% of all forest pixels in the study region). (b) Mean Terra MODIS EVI over rainforests as a function of backscattering fraction evaluated from all 16-day compositing periods in July, August and September (DOY 177 to 272). The backscattering fraction is defined (Morton *et al* 2014) as the fraction of observations with view azimuth less than 90° and greater than 270°. (c) Comparison of model simulated EVI (obtained by digitizing figure 1(c) in Morton *et al* (2014)) with Terra MODIS EVI over Amazonian rainforests. The MODIS EVI is from a 16-day October composite (15th to the 30th) accumulated over 7 seasonal cycles (Section 2.5). The comparison is for phase angles in the range ±10°, that is, ±10° around the hot spot (view zenith angles from 10° to 30° in figure 1(c) of (Morton *et al* 2014)).
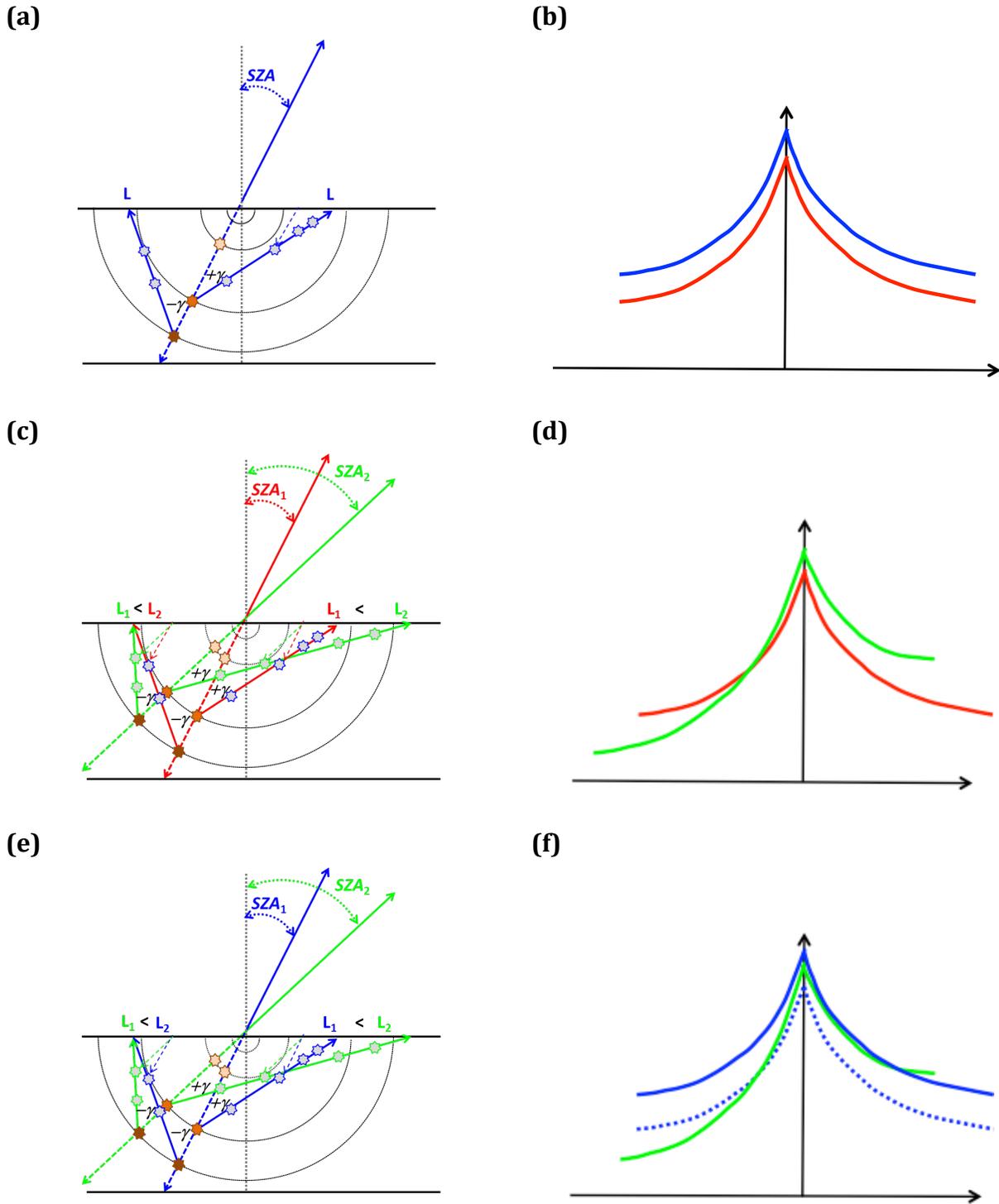
12

Figure S5. Interpretation of angular signatures of reflectance. Illustration of how the angular signature of Bidirectional Reflectance Factors (BRF) is transformed when (a, b) sun-sensor geometry is held invariant but canopy properties are changed; (c, d) sun-sensor geometry is changed but canopy properties are held invariant; (e, f) both sun-sensor geometry and canopy properties are changed. The dashed arrows depict direction of incident parallel beam of unit intensity.
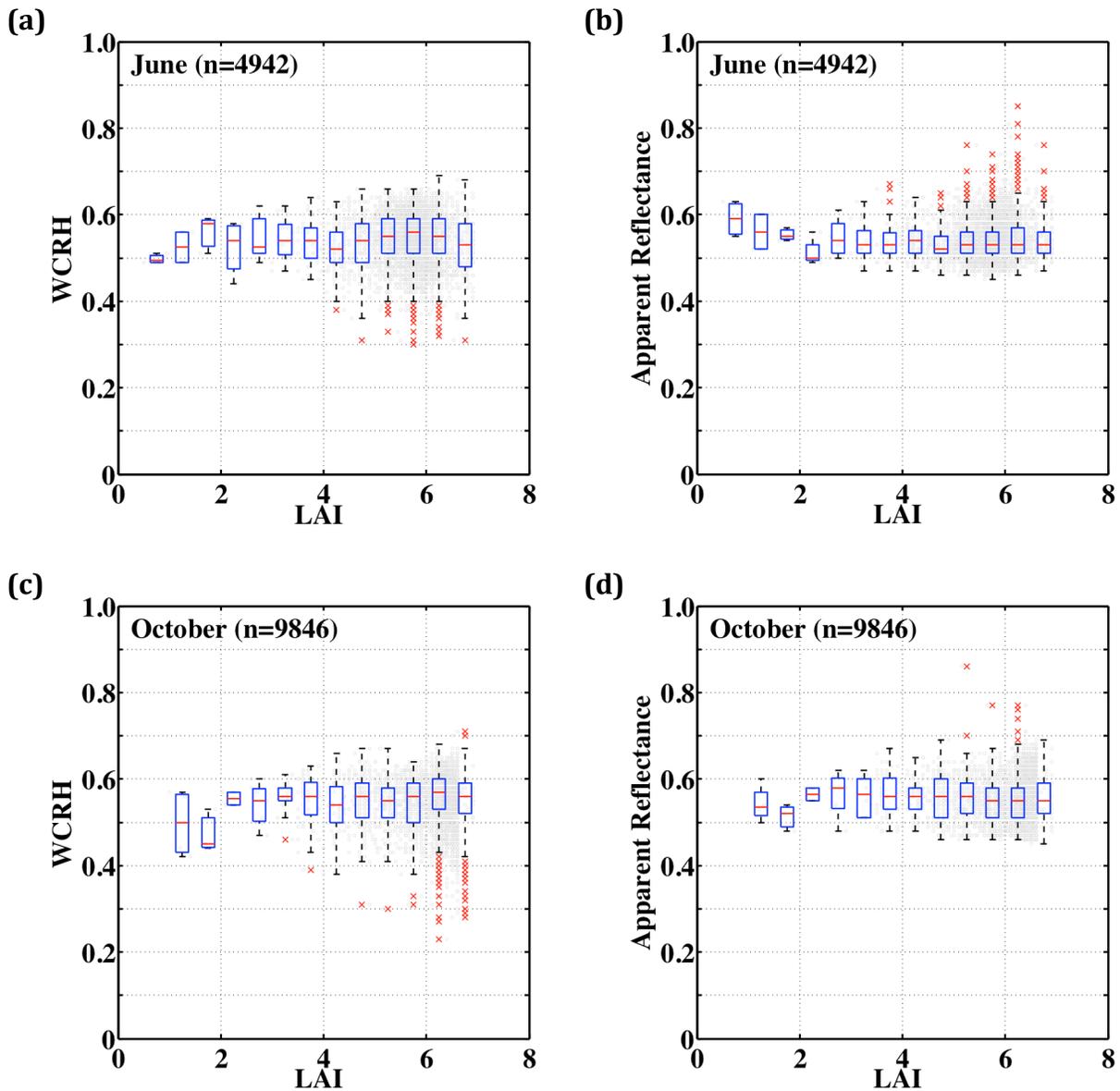
Figure S6. Saturation of GLAS lidar metrics over central Amazonian forests. Distributions of GLAS Waveform Centroid Relative Height (WCRH) and Apparent Reflectance as a function of Terra MODIS LAI in the case of central Amazonian rainforests at the (a, b) beginning and (c, d) end of the dry season. Gray dots and red crosses show distributions of lidar metrics within 0.5 LAI bins. Upper, middle (red line) and lower box edges show the 75%, 50% and 25% percentiles of GLAS metrics. The red crosses are outliers, each representing upper and lower 0.25% of the GLAS lidar observations. June represents data from May-20 to June-23, 2005 and May-24 to June-26, 2006. October represents data from October-3 to November-8, 2004 and October-2 to November-5, 2007. MODIS pixels with valid LAI values and four or more GLAS lidar observations were used (table S3).
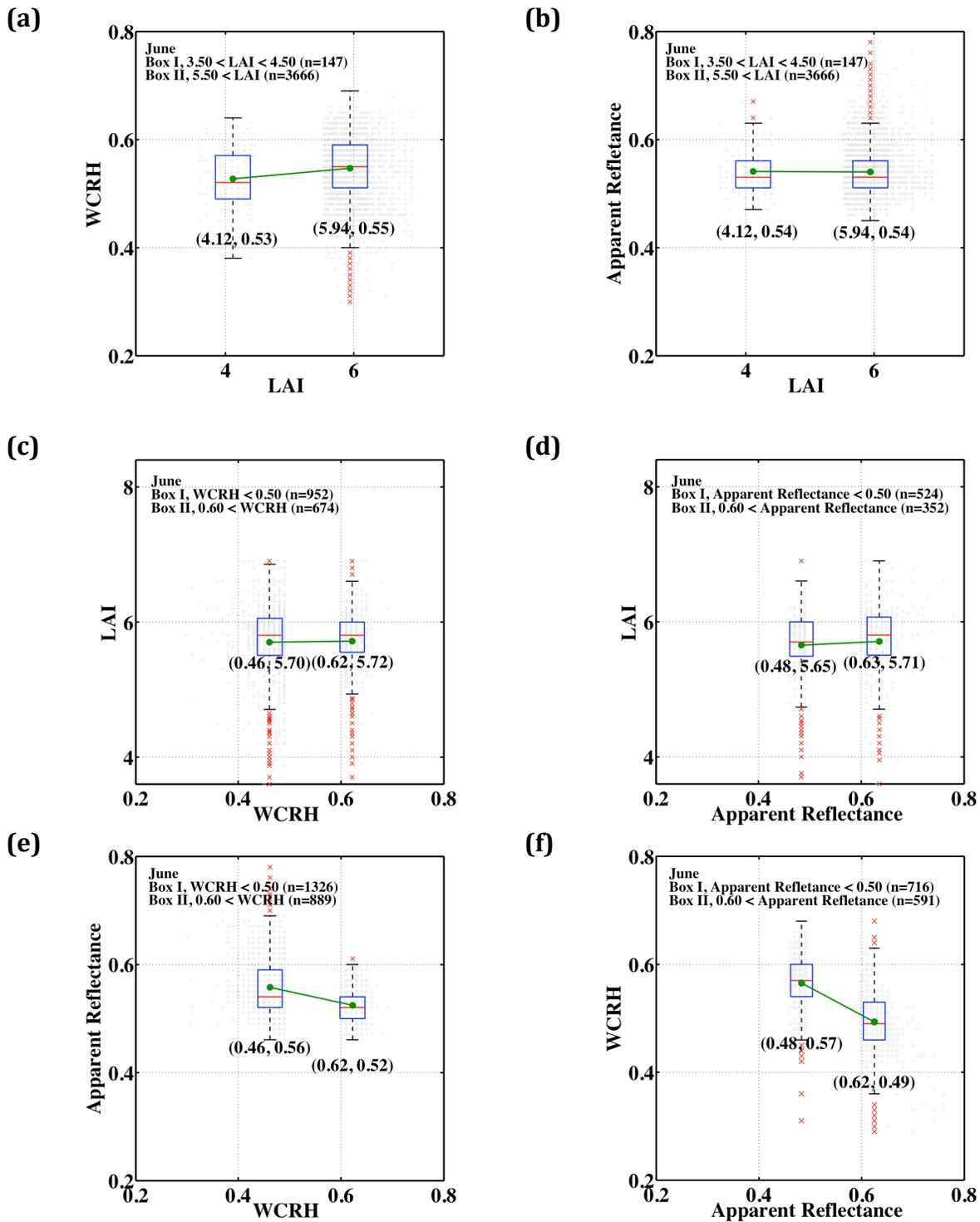
Figure S7. Relationship between GLAS lidar metrics and with LAI. (a, b) Variation in GLAS Waveform Centroid Relative Height (WCRH) and Apparent Reflectance (AR) for pixels with low and high Terra MODIS LAI values. (c, d) Variation in LAI for pixels with low and high values of WCRH and AR. (e, f) Relationship between WCRH and AR. Gray dots and red crosses show the data. Upper, middle (red line) and lower box edges separate the 75%, 50% and 25% percentiles of data used. The red crosses are outliers, each representing upper and lower 0.25% of the data. Similar relations are found for October (not shown).
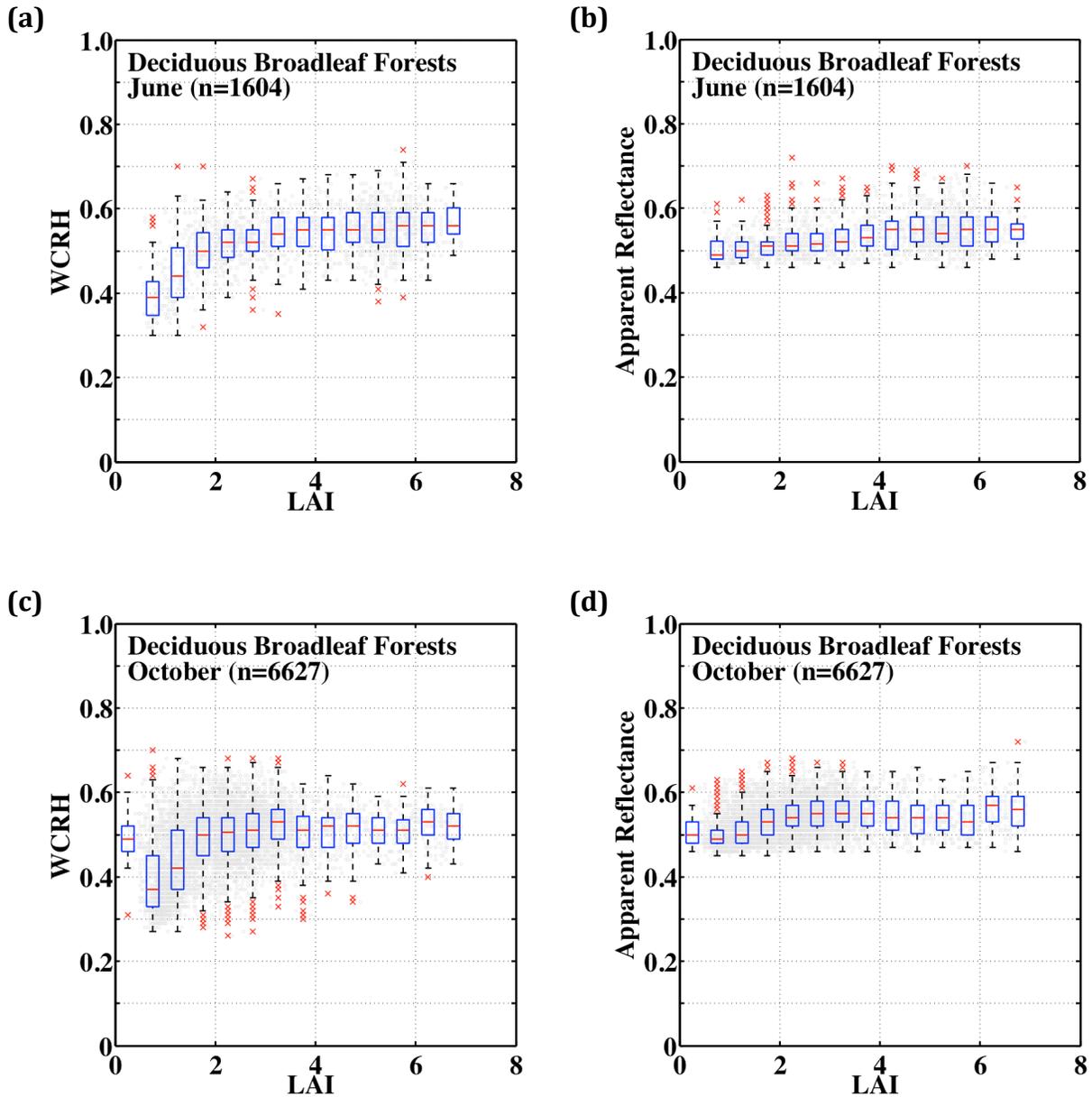
Figure S8. Relationship between GLAS lidar metrics and LAI in deciduous broadleaf forests. Distributions of GLAS Waveform Centroid Relative Height (WCRH) and Apparent Reflectance as a function of Terra MODIS LAI in the case of deciduous (temperate) broadleaf forests in the northern hemisphere in (a, b) June and (c, d) October. Gray dots and red crosses show distributions of lidar metrics within 0.5 LAI bins. Upper, middle (red line) and lower box edges show the 75%, 50% and 25% percentiles of GLAS metrics. The red crosses are outliers, each representing upper and lower 0.25% of the GLAS lidar observations. June represents data from May-20 to June-23, 2005 and May-24 to June-26, 2006. October represents data from October-3 to November-8, 2004 and October-2 to November-5, 2007. MODIS pixels with valid LAI values and four or more GLAS lidar observations were used (table S3).

16

Supplementary Tables

Table S1. Number of greening pixels (Section 1) from Terra and Aqua MODIS sensors

	Terra		Aqua	
Year	Number of greening pixels	As a % of rainforest pixels	Number of greening pixels	As a % of rainforest pixels
2000	804,550	59.02	N/A	N/A
2001	723,796	53.10	N/A	N/A
2002	990,863	72.69	N/A	N/A
2003	518,857	38.06	238,998	17.53
2004	919,820	67.48	233,140	17.10
2005	N/A	N/A	N/A	N/A
2006	901,602	66.14	227,926	16.72
2007	783,164	57.45	260,370	19.10

Table *S2.* Number of pixels with valid EVI and BRF data in June, October and March accumulated over a 7-year period (June 2000 to May 2008, excluding June 2005 to May 2006 due to the dry season drought in 2005) from Terra MODIS and MISR sensors. The table also shows the same for the Aqua MODIS sensor, but accumulated over a 4-year period (June 2003 to May 2008 excluding June 2005 to May 2006)

Sensor	Number of Valid Data	Fraction of Rainforest Pixels With Valid Data (%)		
		June	October	March
Terra MODIS	One or more	96.67	94.38	70.92
Aqua MODIS	One or more	33.65	30.32	12.10
Terra MISR	One or more	48.07	25.75	15.33

Table S3. Number of pixels with valid Terra MODIS LAI data and four or more valid GLAS footprints in June and October

	June		October	
Year	Number of valid LAI pixels	Number of corresponding GLAS footprints	Number of valid LAI pixels	Number of corresponding GLAS footprints
	Amazonian Rainforests			
2004	N/A	N/A	3,859	17,293
2005	3,031	13,536	N/A	N/A
2006	1,911	8,607	N/A	N/A
2007	N/A	N/A	5,987	29,858
Total	4,942	22,143	9,846	47,151
	Deciduous Broadleaf Forests			
2004	N/A	N/A	2,419	10,719
2005	955	4,164	N/A	N/A
2006	649	2,761	N/A	N/A
2007	N/A	N/A	4,208	19,650
Total	1,604	6,925	6,627	30,369

Table S4. Regression relationships between climate and GLAS Waveform Centroid Relative Height (WCRH) and Apparent Reflectance (AR). Climate is represented by annual total precipitation from TRMM, photosynthetically active radiation from CERES and mean annual temperature from CRU. Long-term means of climate variables were evaluated from 2001 to 2010 data, but excluding 2005 and 2010 drought years. Each TRMM pixel contains 10 or more GLAS observations; CERES pixel has 160 or more, and CRU pixel has 40 or more

x	y	Slope	Intercept	R^2	p-value
WCRH	Annual Precipitation (mm year^{-1})	4428.3	297.1	0.17	<0.001
WCRH	Photosynthetically Active Radiation (W m^{-2})	21.8	83.6	0.08	<0.001
WCRH	Mean Annual Temperature (°C)	8.3	22.1	0.15	<0.001
AR	Annual Precipitation (mm year^{-1})	-600.4	3011.2	0.00	0.16
AR	Photosynthetically Active Radiation (W m^{-2})	-65.6	130.9	0.26	<0.001
AR	Mean Annual Temperature (°C)	-10.3	32.1	0.10	<0.001

Table S5. List of Abbreviations

AR	Apparent Reflectance
Aqua	NASA scientific research satellite in a Sun-synchronous near polar circular orbit around the Earth; crosses Equator at 1:30pm
BRF	Bidirectional Reflectance Factor
C5	Collection 5
CERES	Clouds and the Earth's Radiant Energy System
CRU	Climatic Research Unit
DOY	Day of Year (designates the beginning of the compositing period)
ED	Extended Data
EVI	Enhanced Vegetation Index
GLAS	Geoscience Laser Altimeter System
ICESat	Ice, Cloud and land Elevation Satellite
JAS	July, August, and September
LAI	Leaf Area Index
LiDAR	Light Detection and Ranging
MAIAC	Multi-angle Implementation of Atmospheric Correction
MISR	Multiangle Imaging Spectroradiometer
MODIS	Moderate-resolution Imaging Spectroradiometer
NASA	National Aeronautics and Space Administration
NIR	Near Infrared
PA	Phase angle
PAR	Photosynthetically Active Radiation
PDF	Probability Density Function
RAA	Relative Azimuth Angle between solar and sensor view directions
SI	Supplementary Information
SZA	Solar Zenith Angle
SOM	Space Oblique Mercator
Terra	NASA scientific research satellite in a Sun-synchronous near polar circular orbit around the Earth; crosses Equator at 10:30am
TRMM	Tropical Rainfall Measuring Mission
VI	Vegetation Index
VZA	View Zenith Angle
WCRH	Waveform Centroid Relative Height